How to cite: *Angew. Chem. Int. Ed.* **2023**, *62*, e202305041
doi.org/10.1002/anie.202305041

Hydrogen-Bonded Organic Frameworks | Hot Paper

# Tuning Pore Polarization to Boost Ethane/Ethylene Separation Performance in Hydrogen-Bonded Organic Frameworks

*Yunzhe Zhou[+], Cheng Chen[+], Rajamani Krishna, Zhenyu Ji, Daqiang Yuan, and Mingyan Wu**

**Abstract:** Hydrogen-bonded organic frameworks (HOFs) show great potential in energy-saving $C_2H_6/C_2H_4$ separation, but there are few examples of one-step acquisition of $C_2H_4$ from $C_2H_6/C_2H_4$ because it is still difficult to achieve the reverse-order adsorption of $C_2H_6$ and $C_2H_4$. In this work, we boost the $C_2H_6/C_2H_4$ separation performance in two graphene-sheet-like HOFs by tuning pore polarization. Upon heating, an in situ solid phase transformation can be observed from **HOF-NBDA(DMA)** (DMA = dimethylamine cation) to **HOF-NBDA**, accompanied with transformation of the electronegative skeleton into neutral one. As a result, the pore surface of **HOF-NBDA** has become nonpolar, which is beneficial to selectively adsorbing $C_2H_6$. The difference in the capacities for $C_2H_6$ and $C_2H_4$ is 23.4 $cm^3 g^{-1}$ for **HOF-NBDA**, and the $C_2H_6/C_2H_4$ uptake ratio is 136 %, which are much higher than those for **HOF-NBDA(DMA)** (5.0 $cm^3 g^{-1}$ and 108 % respectively). Practical breakthrough experiments demonstrate **HOF-NBDA** could produce polymer-grade $C_2H_4$ from $C_2H_6/C_2H_4$ (1/99, v/v) mixture with a high productivity of 29.2 $L kg^{-1}$ at 298 K, which is about five times as high as **HOF-NBDA(DMA)** (5.4 $L kg^{-1}$). In addition, in situ breakthrough experiments and theoretical calculations indicate the pore surface of **HOF-NBDA** is beneficial to preferentially capture $C_2H_6$ and thus boosts selective separation of $C_2H_6/C_2H_4$.

## Introduction

The polymer-grade ethylene ($C_2H_4 \geq 99.95$ %) is a key feedstock widely used in producing polymers and high-value organic chemicals. In recent years, scientists agree that an economical and energy-efficient alternative purification method is desired to remove the inevitably existing by-product (ethane, $C_2H_6$) from $C_2H_4$.[1,2] The adsorptive separation based on porous materials has attracted extensive attention because of its energy saving and environmental friendliness, excellent reusability and high production efficiency. However, the extremely similar molecular sizes between $C_2H_6$ ($3.81 \times 4.08 \times 4.82$ Å$^3$) and $C_2H_4$ ($3.28 \times 4.18 \times 4.84$ Å$^3$) make it a great challenge for searching appropriate porous materials. Although it has been reported that $C_2H_6/C_2H_4$ separation can be achieved by designing molecular sieve-like materials through pore engineering, it is still very difficult to realize one-step acquisition of high-purity $C_2H_4$.[3–11]

Porous materials featuring nonpolar surfaces have been proven to be certainly beneficial for trapping $C_2H_6$ molecules and can be consequently regarded as good candidates for $C_2H_6$-selective adsorbent.[12–18] Hydrogen-bonded organic frameworks (HOFs) self-assembled by conjugated organic carboxylic acids through intermolecular hydrogen-bonding interactions usually have regulatable nonpolar channels and can be deemed to be potential $C_2H_6$-selective materials.[12,19–21] Recently, molecular building blocks based on organic carboxylic acids have been developed for unveiling the self-assembly rules of HOFs to a certain extent through backbone geometry and directional dimeric hydrogen-bonding regulation.[19,22–25] However, effective rules for rational design and self-assembly of HOFs have not been clearly established. In part, this is due to its fragile nature and poor rigidity of hydrogen bonding, allowing frameworks to often collapse after removal of guest molecules.[22,26] Common solvents such as alcohols will form O–H···O and/or N–H···O interactions during the HOFs synthesis process, occupying a certain space in the channels or even leading to structural collapse after activation.[26] In particular, the dimethylamine molecules generated in the synthesis process can seize the hydrions of the carboxylic acids to form electropositive dimethylamine cations and further form hydrogen bond interactions with the carboxylate groups on the electronegative framework, which results in high polarity in the HOFs.[24] As we know, highly polar pore surfaces will simultaneously enhance the affinity for both $C_2H_6$ and $C_2H_4$

[*] Y. Zhou,[+] Dr. C. Chen,[+] Dr. Z. Ji, Prof. Dr. D. Yuan, Prof. Dr. M. Wu
State Key Lab of Structural Chemistry, Fujian Institute of Research on the Structure of Matter, Chinese Academy of Sciences
Fuzhou, Fujian 350002 (China)
E-mail: wumy@fjirsm.ac.cn

Prof. R. Krishna
Van't Hoff Institute for Molecular Sciences, University of Amsterdam
Science Park 904, 1098 XH Amsterdam (The Netherlands)

Prof. Dr. M. Wu
University of Chinese Academy of Sciences
Beijing, 100049 (China)

[+] These authors contributed equally to this work.

molecules, which cannot efficiently discriminate $C_2H_6$ from $C_2H_6$ and $C_2H_4$ mixture. The good news, however, is that dimethylamine cations can be removed by thermal and/or vacuum activation, which will significantly reduce the polarity of the pore surface. Though the nonpolar pore surfaces will weaken the affinity for both $C_2H_6$ and $C_2H_4$ simultaneously, the selective adsorption of $C_2H_6$ can be realized. The reason is that the $C_2H_6$ molecule has a higher polarizability ($44.7\times10^{-25}$ $cm^3$) than $C_2H_4$ ($42.52\times10^{-25}$ $cm^3$), which renders it stronger interactions with the nonpolar pore surfaces that are full of aromatic moieties, wherein dispersion and induction interactions may afford major contribution to the preferential adsorption of $C_2H_6$ over $C_2H_4$.[24,25,27] Therefore, one-step acquisition of pure $C_2H_4$ from $C_2H_6/C_2H_4$ mixture can be realized.

Based on the above considerations, we herein report a strategy of tuning pore polarization to successfully convert highly polar pore surfaces featuring –COOH···$^-$OOC– carboxyl dimers into less polar pore surfaces with head-to-head carboxyl···carboxyl dimers through in situ solid transformation, which realizes the enhancement of one-step $C_2H_6/C_2H_4$ separation performance. Under solvothermal condition, the propeller-like hexarboxylic acid 4′,4″,4‴-nitrilotris(([1,1′-biphenyl]-3,5-dicarboxylic acid)) (abbreviated as $H_6$NBDA) is employed to synthesize a hydrogen-bonded organic framework (**HOF-NBDA(DMA)**, DMA = dimethylamine cation), in which deprotonated $H_5$NBDA unit self-assembles into 2D graphene-sheet-like nets through intermolecular hydrogen bonds under the rule of reticular chemistry.[28–31] Furthermore, the electronegative layers are stacked in -ABCD- manner without interpenetration to form the 1D open channels along the crystallographic *a*-axis, where DMA molecules reside. Upon heating, **HOF-NBDA-(DMA)** can transform in situ into **HOF-NBDA** by loss of dimethylamine molecules ($Me_2NH$). Therefore, **HOF-NBDA** has nonpolar pore surfaces, which are stacked by electrically neutral 2D net constructed from $H_6$NBDA unit. As anticipated, **HOF-NBDA(DMA)** shows an unobvious difference in $C_2H_6$ and $C_2H_4$ adsorption capacity as $5.0\ cm^3\,g^{-1}$ between $C_2H_6$ and $C_2H_4$, while **HOF-NBDA** shows the preferential adsorption of $C_2H_6$ over $C_2H_4$ (the difference in adsorption capacity increases to $23.4\ cm^3\,g^{-1}$). Furthermore, **HOF-NBDA** exhibits a significantly higher $C_2H_6/C_2H_4$ (1/99, v/v) selectivity (1.75) than that of **HOF-NBDA(DMA)** (1.40). Practical breakthrough experiments show that **HOF-NBDA(DMA)** exhibits an inefficient separation of the $C_2H_6/C_2H_4$ mixture with a interval of ca. $3.1\ min\,g^{-1}$. In contrast, **HOF-NBDA** could efficiently capture $C_2H_6$ from 1/99 $C_2H_6/C_2H_4$ mixture at different gas flow rates and temperatures, providing polymer-grade $C_2H_4$ in a significantly prolonged separation interval ($15.5\ min\,g^{-1}$), which is five times longer than that of **HOF-NBDA(DMA)** under the same conditions. The **HOF-NBDA** packed column can directly yield in a high $C_2H_4$ productivity of $29.2\ L\,kg^{-1}$ at 298 K and 1 bar, which is about five times as high as **HOF-NBDA(DMA)** ($5.4\ L\,kg^{-1}$). In addition, in situ breakthrough experiments indicate the $C_2H_6/C_2H_4$ separation performance is greatly improved accompanied with the gradual heat treatment. Finally, theoretical calculations indicate that the pore surface of **HOF-NBDA** is beneficial to preferentially capture $C_2H_6$ rather than $C_2H_4$ and thus boosts selective separation of $C_2H_6/C_2H_4$, which is well consistent to the experimental result. On the whole, these results not only provide in-depth insights into conceivable reticular chemistry of HOFs platform, but also guide hydrogen bonding as a mainstream non-covalent interaction to fabricate artificial porous materials with selective separation properties in the field of energy-saving gas purification.[12,19–21,23,24,32–38]

## Results and Discussion

The hexacarboxylate skeleton $H_6$NBDA was obtained through a multi-step synthesis reaction (Scheme S1, Figure S1, Supporting Information). A solvothermal reaction for three days afforded the yellow block crystals of **HOF-NBDA(DMA)**. Single-crystal X-ray diffraction (SCXRD) analysis revealed that **HOF-NBDA(DMA)** belongs to the monoclinic *P*-1 space group (Table S3). The asymmetric unit of **HOF-NBDA(DMA)** consists of two deprotonated $H_5$NBDA units and two DMA (Figure S2a). Each $H_5$NBDA unit is connected to three adjacent $H_5$NBDA units through six sets of intermolecular hydrogen bonds to extend into 2D honeycomb-like layers. Among them, four are classical carboxyl···carboxyl dimers (∠O–H···O ranging from 169.8° to 177.8°, d (O–H···O) ranging from 2.46 to 2.63 Å.) (H-1, Figure 1b and S3a). And the other two are rarely-seen -COOH···$^-$OOC- hydrogen bonds (∠N–H···O recorded as 146.4° and 148.2°, d (N–H···O) recorded as 2.69 Å and 2.72 Å.) (H-2, Figure 1b and S3a). It is worth noting that the 2D layers skeleton is overall electronegative, and DMA is connected to the $COO^-$ of the skeleton by N–H···O hydrogen bonds, thus maintaining the overall electroneutrality. In the 2D layer, there are three kinds of windows (I, II and III, See Figure 1b) and the DMA are distributed in type I window. Interestingly, the layered frameworks are stacked in parallel in a rarely seen -ABCD- manner without interpenetration to form the 1D open channels along the crystallographic a-axis, with an average interlayer distance of ca. 3.68 Å (Figure 2a and S4a).

When degassed under dynamic vacuum, the block **HOF-NBDA(DMA)** crystals split into many pieces. Fortunately, the tiny activated samples also meet the requirements for SCXRD investigations. Therefore, the accurate structure of **HOF-NBDA** was successfully obtained. **HOF-NBDA** belongs to the orthorhombic *F*ddd space group. The asymmetric unit of **HOF-NBDA** contains a half $H_6$NBDA molecule, which is not deprotonated (Figure S2b). Each $H_6$NBDA molecule is hydrogen bonded with three adjacent $H_6$NBDA exclusively through carboxyl…carboxyl dimers (∠O–H···O record as 179.2° and 176.2°, d (O–H···O) record as 2.60 and 2.62 Å, respectively) in the *bc* plane to form an electrically neutral 2D hexagonal honeycomb net (H-1, Figure 1c and S3b). Compared with **HOF-NBDA(DMA)**, the 2D layer of **HOF-NBDA** consists of two types of windows, i.e. type II and the larger type IV which is constructed by six isophthalate groups (Figure 1c). Similar to **HOF-NBDA-**

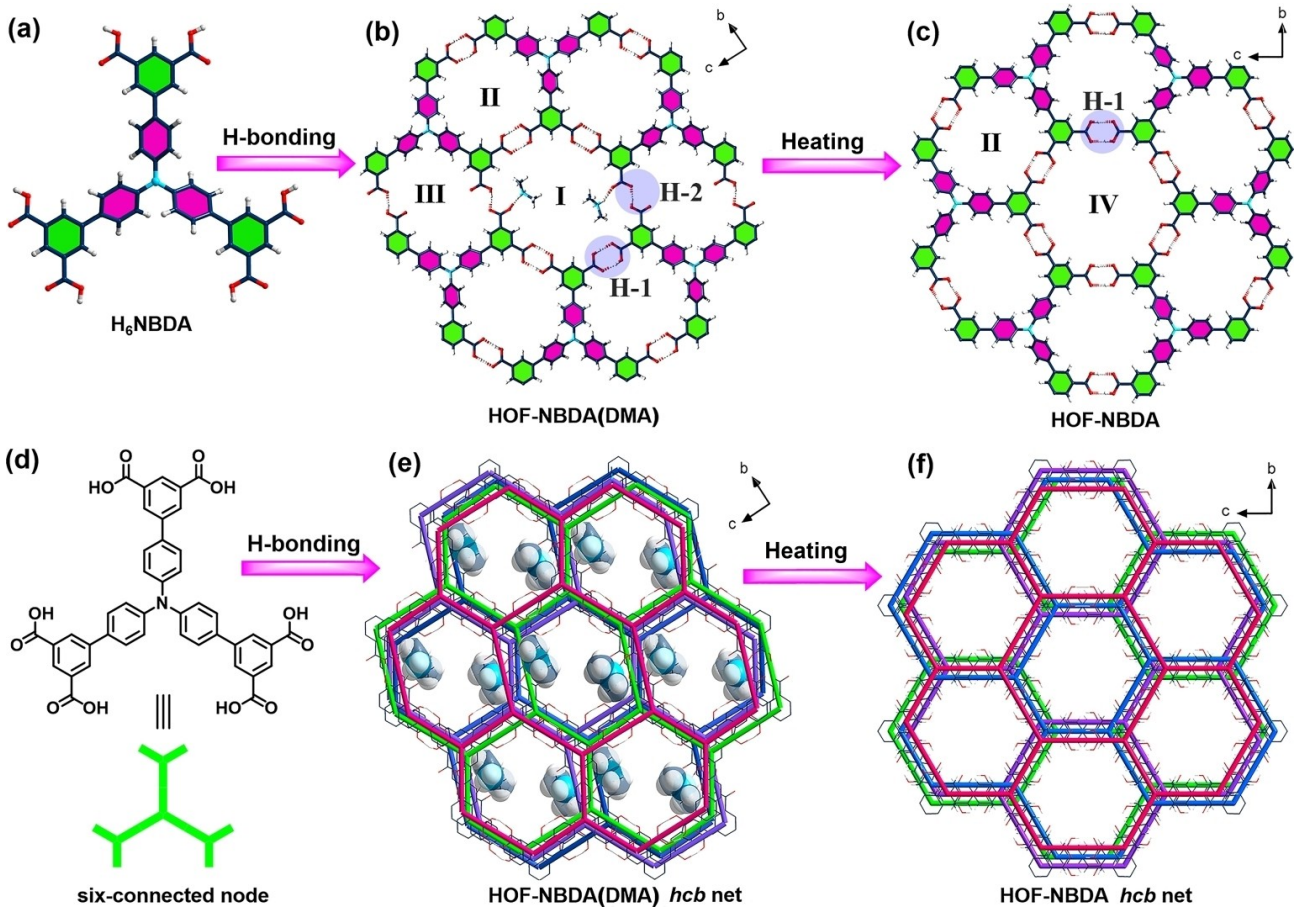


***Figure 1.*** (a) The molecular structure of $H_6$NBDA. (b) Representation of the three kinds of hexagonal windows (named as I, II and III, respectively), and the resulting monolayer network in **HOF-NBDA(DMA)**. (c) Upon heating, **HOF-NBDA(DMA)** in situ transforms into **HOF-NBDA**, accompanied with the removal of dimethylamine molecules and the reorganization of hydrogen bond dimers. (d) Scheme of $H_6$NBDA molecule and its simplified six-connected model. (e) For **HOF-NBDA(DMA)**, the layered frameworks are stacked in a -ABCD- manner without interpenetration, with the dimethylamine cations distributed in the pores. (f) The stacking structure of **HOF-NBDA**.

**(DMA)**, the 2D layers of **HOF-NBDA** are also stacked in a -ABCD- manner without interpenetration (an interlamellar separation of 3.73 Å, Figures 1f, 2b and S4b), resulting in a 1D channel along the *a*-axis. Compared with the wavelike layers constructed by rigid aromatic tricarboxylated ligands (such as $H_3$BTB and $H_3$TATB),[22,39] the propeller-like hexarboxylic acid $H_6$NBDA derived from triphenylamine scaffolder can facilitate the formation of slip-packed 2D layered structures that are more similar to the free-standing graphene sheets.[40]

Hirshfeld surface analysis demonstrates that the electrostatic potential (ESP) on the pore walls is significantly different between **HOF-NBDA(DMA)** and **HOF-NBDA**. A lot of positive charge centers are formed in the DMA occupied pores (Figure 2c), which will increase the adsorption affinity of both $C_2H_6$ and $C_2H_4$ molecules simultaneously due to strong intermolecular electrostatic interactions. Such polar pore surfaces make it difficult to achieve efficient selective separation of $C_2H_6/C_2H_4$ mixture. However, in **HOF-NBDA** the pore surface becomes less polar, and the abundant phenyls and the consolidated carboxyl···carboxyl dimers on the pore walls benefit the preferential adsorption of $C_2H_6$ molecules (Figure 2d). Such great difference in charge density distribution of the pore surface in these two crystals will bring special influence on their adsorption properties (Figure S5).

Both **HOF-NBDA(DMA)** and **HOF-NBDA** are composed of hexagonal network framework stacked in -ABCD- manner, and possess similar 2D layered graphene-sheet-like topological structure. The main difference between the two structures is the existence of DMA filled in the channels of the **HOF-NBDA(DMA)** framework. Whereas DMA will decompose at high temperature and the resulting $Me_2NH$ can be removed from the pores by vacuum.[41] Further experiments have been conducted to investigate this possibility. As expected, it was found that the powder X-ray diffraction (PXRD) peaks changed obviously and matched well to the **HOF-NBDA** pattern when the **HOF-NBDA-(DMA)** sample was activated by heating in air or under vacuum (Figure S6), which indicated a possible solid-state structural transformation. Therefore, freshly prepared bulk crystalline powder for in situ monitoring the solid-state transformation was measured on a Rigaku MiniFlex600 diffractometer after heating at different temperatures. As

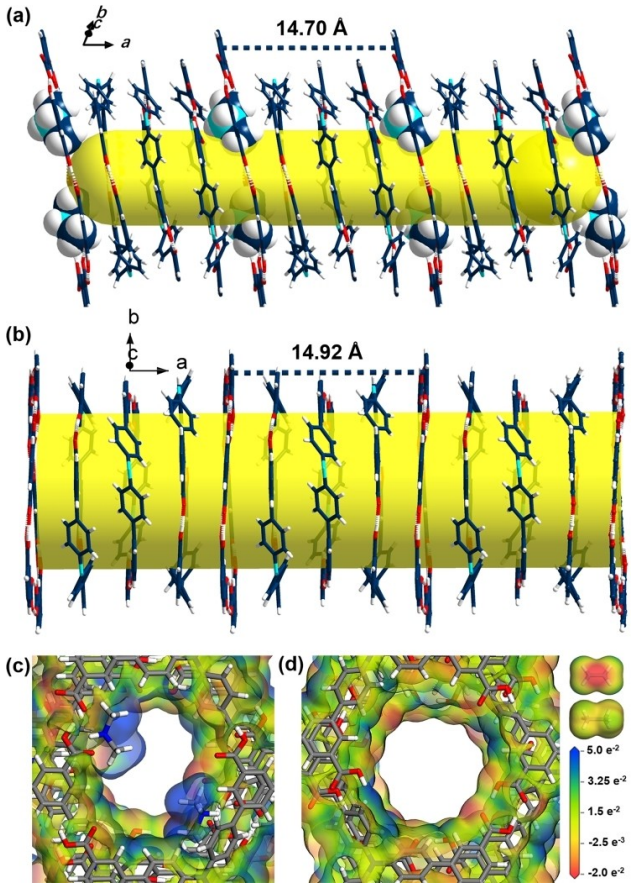


***Figure 2.*** A cross-section view of the hexagonal porous windows in (a) **HOF-NBDA(DMA)** and (b) **HOF-NBDA**. The layered frameworks are stacked in slippage in a -ABCD- manner without interpenetration with average interlayer distances of ca. 3.68 and 3.73 Å, respectively. The steric electrostatic potential on the hexagonal channels of (c) **HOF-NBDA(DMA)** and (d) **HOF-NBDA**. The gradation on the scale bar is in Hartree/e.

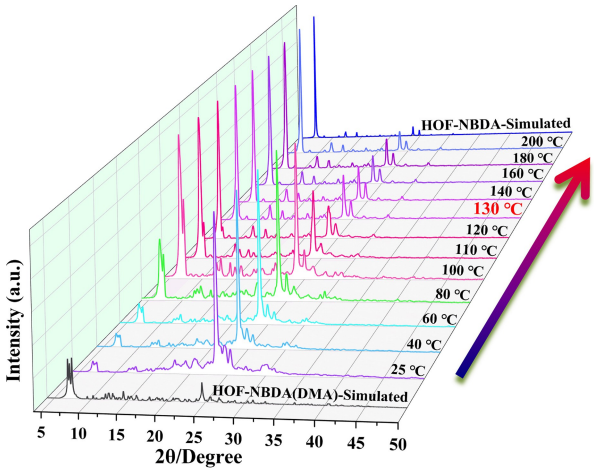


***Figure 3.*** PXRD patterns collected after continual heating treatments at different temperatures confirm the in situ structural transformation from **HOF-NBDA(DMA)** to **HOF-NBDA**.

shown in Figure 3, the as-prepared **HOF-NBDA(DMA)** shows no obvious change before 80 °C. When the temperature rises to 130 °C, the curves have pronounced changes. Especially the peaks located at 6.9° and 7.5° gradually weaken and completely disappear, and the peak located at 7.1° becomes a single independent peak when the temperature rises to 130 °C, as well as a new peak appears at 8.6°. Under this heating condition, the **HOF-NBDA(DMA)** sample is successfully converted to **HOF-NBDA** as evidenced by the consistency in their corresponding PXRD patterns. Continuous heat treatment does not result in any signal change, even when the temperature reaches 200 °C, indicating the occurrence of completely heat-induced structural transformation (Figure 3). In a word, we have achieved the removal of DMA and the reorganization of carboxyl···carboxyl dimers through in situ heating, and then realized the strategy of tuning pore polarization by changing the porous surface charge density distribution.

What makes sense is that the **HOF-NBDA** can be synthesized on a large scale in the laboratory by rapid synthesis methods (Figure S6), which greatly improves the application possibilities of the material. The scanning electron microscope photographs show that the rapidly scale-up synthesized **HOF-NBDA** crystals are block and about 10 μm in size with an irregular polygonal shape (Figure S7). In addition, the high stability of materials is also a prerequisite for their practical application. **HOF-NBDA** shows exceptional chemical stability and maintains its crystallinity upon exposure to some common chemical solvents, such as EtOH, acetone, $CH_3CN$, and $CHCl_3$ etc. at room temperature (Figure S8). Even treated in boiling water or harsher chemical environment such as 12 M HCl for 24 h, their corresponding PXRD patterns are also consistent with the simulated ones (Figure S9). It also can be witnessed that there are almost unchanged in the variable-temperature PXRD patterns that measured up to 200 °C in air atmosphere (Figures S10–S11, Table S4). The above experiments demonstrated the excellent thermal stability of both the in situ transformed crystalline **HOF-NBDA** and the quickly synthesized samples in large quantity.

The permanent porosities of **HOF-NBDA(DMA)** and **HOF-NBDA** were disclosed by $N_2$ sorption measurement. $N_2$ isotherm at 77 K shows that **HOF-NBDA(DMA)** possesses typical type I sorption profile and takes up the $N_2$ amount of 168 $cm^3 g^{-1}$ at 1 bar, confirming its microporous nature with the BET surface area of 590 $m^2 g^{-1}$ (Figure 4a). In contrast, analysis by the PLATON program[42] shows that about 40.5 % of the volume in **HOF-NBDA** is solvent-accessible after removing $Me_2NH$ in the pores, which is much higher than that of **HOF-NBDA(DMA)** (about 31.5 %). As anticipated, **HOF-NBDA** by scale-up synthesis shows good adsorption behavior for nitrogen, and takes up 297 $cm^3 g^{-1}$ $N_2$ at 77 K and 1 bar. The isotherm also exhibits the type I sorption behavior and the BET surface area of **HOF-NBDA** is calculated to be 965 $m^2 g^{-1}$, which is also much higher than that of **HOF-NBDA(DMA)**. More importantly, $N_2$ adsorption isotherms show that $N_2$ uptake of **HOF-NBDA** have only a slight decrease (279, 275 and 284 $cm^3 g^{-1}$, respectively) after harsh treatments such as

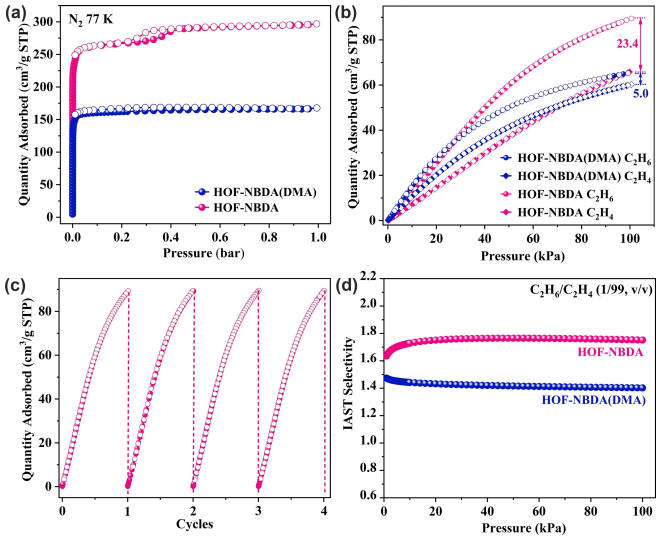


***Figure 4.*** (a) $N_2$ adsorption isotherms of **HOF-NBDA** and **HOF-NBDA-(DMA)** at 77 K. (b) Adsorption isotherms of $C_2H_6$ and $C_2H_4$ of **HOF-NBDA(DMA)** (blue line) and **HOF-NBDA** (red line) at 298 K respectively. (c) $C_2H_6$ sorption cycles for **HOF-NBDA** at 298 K. (d) $C_2H_6/C_2H_4$ (1/99, v/v) IAST selectivity of **HOF-NBDA** and **HOF-NBDA(DMA)** at 298 K.

being evacuated at 180 °C for 3 h, being soaked in boiling water for 24 h and 12 M HCl for 24 h (Figure S12). These results indicate that **HOF-NBDA** possesses excellent structural robustness which is consistent with the PXRD results and has potential application in the gas adsorption and separation.

Examination of the single-component adsorption isotherms of $C_2H_6$ and $C_2H_4$ at 298 and 273 K was carried out after corroborating the permanent porosity in **HOF-NBDA-(DMA)** and the robust **HOF-NBDA**. Interestingly, both these two materials have successfully realized the reverse-order characteristic $C_2H_6/C_2H_4$ adsorption. As shown in Figure 4b, the $C_2H_6$ uptake amount (65.2 $cm^3 g^{-1}$) of **HOF-NBDA(DMA)** is slightly higher than that of $C_2H_4$ (60.2 $cm^3 g^{-1}$) at 298 K and 100 kPa, affording an adsorption amount difference of 5.0 $cm^3 g^{-1}$, and an $C_2H_6/C_2H_4$ uptake ratio of 108 %. In comparison, **HOF-NBDA** exhibits an obviously preferential adsorption of $C_2H_6$ over $C_2H_4$ during the entire range of 1 bar (Figure 4b). **HOF-NBDA** displays an extremely high loading of $C_2H_6$ (89.2 $cm^3 g^{-1}$) at 298 K, which is 1.4 times higher than that of **HOF-NBDA(DMA)**. In addition, for **HOF-NBDA** the $C_2H_6$ uptake is much higher than that of $C_2H_4$ (65.8 $cm^3 g^{-1}$), resulting an adsorption amount difference of 23.4 $cm^3 g^{-1}$, and a greatly enlarged $C_2H_6/C_2H_4$ uptake ratio of 136 %. Such preferential adsorption of $C_2H_6$ over $C_2H_4$ is also monitored at 273 K (Figure S13). Cyclic tests demonstrate that **HOF-NBDA** can be facilely reactivated and the sorption isotherms of $C_2H_6$ have no obvious decrease after four cycles (Figure 4c). The experimental isosteric heats ($Q_{st}$) difference values between $C_2H_6$ and $C_2H_4$ for **HOF-NBDA(DMA)** and **HOF-NBDA** are increased from 2.2 to 3.6 kJ $mol^{-1}$, which indicates that the separation performance for $C_2H_6$ and $C_2H_4$ is significantly enhanced after the structure transformation (Figure S14). The $C_2H_6$ uptake of **HOF-NBDA** (3.98 mmol $g^{-1}$) at 1 bar and 298 K is notably higher than those of benchmark HOF-BTB (3.09 mmol $g^{-1}$),[43] ZJU-HOF-10 (2.19 mmol $g^{-1}$),[20] HIAM-102 (2.15 mmol $g^{-1}$),[21] and HOF-76a (2.95 mmol $g^{-1}$),[12] but is slightly less than ZJU-HOF-1 (4.87 mmol $g^{-1}$).[19] Furthermore, the $C_2H_6/C_2H_4$ uptake ratio (136 %) of **HOF-NBDA** at 1 bar outperforms most of the reported $C_2H_6$-selective HOFs materials except HOF-76a (177 %), further proving its excellent selectivity (Table S5). Based on the remarkable reverse-order $C_2H_6/C_2H_4$ adsorption, we further calculated the separation performance of these two HOFs at 298 K by the ideal adsorbed solution theory (IAST). For **HOF-NBDA**, with increasing pressure, the final IAST selectivity of $C_2H_6/C_2H_4$ (1/99, v/v) at 298 K is 1.75 (Figure 4d), which is higher than that of **HOF-NBDA-(DMA)** (1.40). The value is larger than the reverse-order characteristic HOF-BTB (1.4), and is comparable to ZJU-HOF-10 (1.9), HIAM-102 (1.9), HOF-76a (2.0), and ZJU-HOF-1 (2.25) (Figure S15 and Table S5). Overall, the above results clearly show that through tuning pore polarization the uptake of $C_2H_6$, the $C_2H_6/C_2H_4$ uptake ratio as well as the $C_2H_6/C_2H_4$ selectivity has been greatly improved. Significantly, **HOF-NBDA** is one of the outstanding $C_2H_6$-selective HOFs materials reported and may serve as the high-efficiency adsorbent for one-step acquisition of $C_2H_4$ from $C_2H_6/C_2H_4$ mixture.

In order to further verify that the strategy of tuning pore polarization is beneficial for practical $C_2H_6/C_2H_4$ separation, practical breakthrough experiments of the feed gas $C_2H_6/C_2H_4$ in a volume ratio of 1/99 are conducted with a flow rate of 2 mL $min^{-1}$ at 298 K. Firstly, the breakthrough experiments were performed with **HOF-NBDA(DMA)**. As shown in Figure 5a, $C_2H_4$ flows out of the **HOF-NBDA-(DMA)** packed column firstly at 33.4 min $g^{-1}$, and the $C_2H_6$ is quickly detected at a small interval of ca. 3.1 min $g^{-1}$. The production of pure $C_2H_4$ from the $C_2H_6/C_2H_4$ (1/99, v/v) mixture by **HOF-NBDA(DMA)** adsorbent is calculated to be 5.4 L $kg^{-1}$. Obviously, **HOF-NBDA(DMA)** is not a good adsorbent for one-step separation of the $C_2H_6/C_2H_4$ mixture. However, for **HOF-NBDA** the $C_2H_4$ elutes through the fixed bed first at ca. 47.5 min $g^{-1}$ to yield an outflow of polymer-grade gas ($C_2H_4 \geq 99.95$ %) with the undetectable amount of $C_2H_6$ (the detection limit of the GC instrument is 100 ppm). Subsequently, the $C_2H_6$ breaks through the adsorption bed at ca. 63.0 min $g^{-1}$ because $C_2H_6$ molecules are more efficiently adsorbed. As a result, there is a significant interval of 15.5 min $g^{-1}$ between $C_2H_4$ and $C_2H_6$ experimental breakthrough times, which is about five times as many as **HOF-NBDA(DMA)**. It is worth mentioning that this result is consistent with the simulated one (ca. 16.5 min $g^{-1}$) (Figure S16). In addition, the production of pure $C_2H_4$ from the $C_2H_6/C_2H_4$ (1/99, v/v) mixture for **HOF-NBDA** adsorbent is ca. 29.2 L $kg^{-1}$, which is about four times higher than that of **HOF-NBDA(DMA)** and is in accord with the transient breakthrough simulations (31.1 L $kg^{-1}$). Furthermore, the breakthrough experiments for **HOF-NBDA** with other $C_2H_6/C_2H_4$ mixtures (1/15 and 1/9 $C_2H_6/C_2H_4$) are also carried out (Figure S17–S21). As

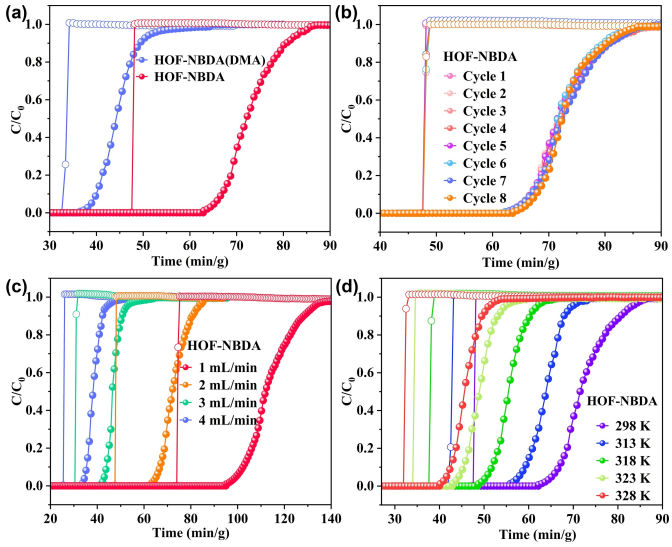


***Figure 5.*** (a) Experimental breakthrough curves for $C_2H_6/C_2H_4$ (1/99, v/v) mixture in freshly prepared **HOF-NBDA(DMA)** (blue) and rapid synthesized **HOF-NBDA** (red) packed columns respectively with gas flow rate of the 2 mL min$^{-1}$ at 298 K. (b) The cycling breakthrough experiment tests for a $C_2H_6/C_2H_4$ (1/99, v/v) mixture with gas flow rate of the 2 mL min$^{-1}$ at 298 K. (c) Experiment breakthrough experiments under different gas flow rates at 298 K. (d) The breakthrough experiment under different temperatures with gas flow rate of the 2 mL min$^{-1}$.

seen in Figure S17 and S18, for 1/15 and 1/9 $C_2H_6/C_2H_4$ mixtures, pure $C_2H_4$ first elutes through the column and the seperation intervals are 10.4 and 10.2 min g$^{-1}$ respectively, which match well with the simulated ones (11.4 and 11.3 min g$^{-1}$). It is obvious that through tuning pore polarization **HOF-NBDA** which has nonpolar pore surfaces realizes the efficient $C_2H_6/C_2H_4$ separation. To our surprise, **HOF-NBDA** can keep the separation performance after several continuous measurement cycles, indicating its outstanding recyclability for $C_2H_6/C_2H_4$ separation (Figure 5b and Figures S19–S20). Additionally, as shown in Figures 5c-d, effective separation of $C_2H_6/C_2H_4$ can be achieved in breakthrough measurements at different gas flow rates (1 to 4 mL min$^{-1}$, respectively) and different temperatures (298, 313, 318, 323 and 328 K), which indicate that **HOF-NBDA** can achieve the one-step separation of $C_2H_6/C_2H_4$ mixtures in the complex working conditions.

To get a deeper understanding of the separation effect caused by the pore polarization changes, we performed a series of continual breakthrough experiments on a **HOF-NBDA(DMA)** packed adsorption bed. Following by the in situ programmed heating process, **HOF-NBDA(DMA)** experienced a solid transformation to **HOF-NBDA**, and the corresponding separation performance for $C_2H_6/C_2H_4$ (1/99, v/v) mixture was real-time monitored. As expected, increasing activation temperature, **HOF-NBDA(DMA)** is gradually transformed into **HOF-NBDA**, and the separation time intervals of $C_2H_6/C_2H_4$ (1/99, v/v) mixture are getting longer. When the packed column is gradually heated from 40 to 160 °C, the breakthrough time intervals are increased from 7.2 to 25.6 minutes (calculated as 14.4 min g$^{-1}$ by mass ratio) between $C_2H_4$ and $C_2H_6$, which is 4.6 times as much as that of original **HOF-NBDA(DMA)** (Figure 6). The PXRD patterns and the $^1$H NMR spectrum confirm that **HOF-NBDA(DMA)** completely transforms to **HOF-NBDA** finally (Figures S1 and S6). These results indicate the in situ thermal activation can not only promote the complete structural transformation, which changes the pore polarity but also boost the $C_2H_6/C_2H_4$ separation efficiency simultaneously.

To gain precise insight into the binding sites of ethane and ethylene in HOFs, we performed calculations using Grand Canonical Monte Carlo (GCMC) method (Figure 7). In **HOF-NBDA(DMA)**, $C_2H_6$ molecule interacts with two phenyl rings and three carboxylic oxygen atoms to form triple C–H···π interactions (H···π distances, 3.54, 4.19 and 4.23 Å; corresponding C···C separations, 3.56, 3.72 and 3.87 Å, respectively) and triple C–H···O interactions (H···O distances, 2.78, 2.80 and 2.91 Å, respectively).[12,19,44] The planar $C_2H_4$ molecule shows two strong C–H···O interactions (H···O distances, 2.52 and 2.56 Å, respectively) as well as electrostatic interactions with an adjacent DMA and a phenyl ring (corresponding C···C separations, 3.88, 3.46 and 3.57 Å, respectively).[12,19,45,46] The corresponding static binding energies of **HOF-NBDA(DMA)** for $C_2H_6$ and $C_2H_4$ molecules are calculated as 43.2 and 40.2 kJ mol$^{-1}$, with a difference in value of 3.0 kJ mol$^{-1}$. As shown in Figures 7c and 7d, for **HOF-NBDA**, $C_2H_6$ molecule slightly stands up in the pore to form three C–H···π interactions with the nearest phenyl ring (H···π distances from 2.95 to 4.32 Å), as well as the C···C separations (3.66, 3.86 and 3.99 Å, respectively). There are also quadruple C–H···O interactions and the H···O distances are calculated to be 2.64, 2.77, 3.16 and 3.18 Å. In comparison, the $C_2H_4$ molecule laid flat in the channel and showed only three C–H···O interactions (H···O distances, 2.88, 2.90 and 2.92 Å, respectively), as well as electrostatic interactions between its planar skeleton and two adjacent phenyl rings (corresponding C···C separations, 3.88 and 3.98 Å, respectively). The corresponding static binding energies of **HOF-NBDA** for $C_2H_6$ and $C_2H_4$

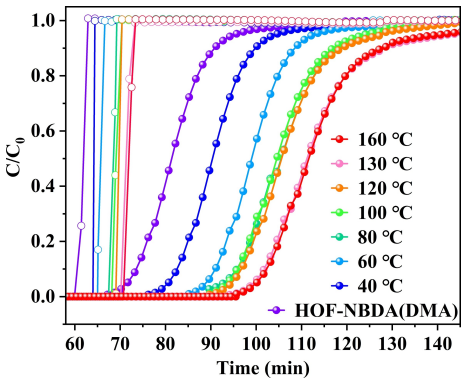


***Figure 6.*** Experimental breakthrough curves for $C_2H_6/C_2H_4$ (1/99, v/v) mixture (gas flow rate of 2 mL min$^{-1}$) in the real-time monitoring of a packed column with in situ transformation of **HOF-NBDA(DMA)** to **HOF-NBDA**.

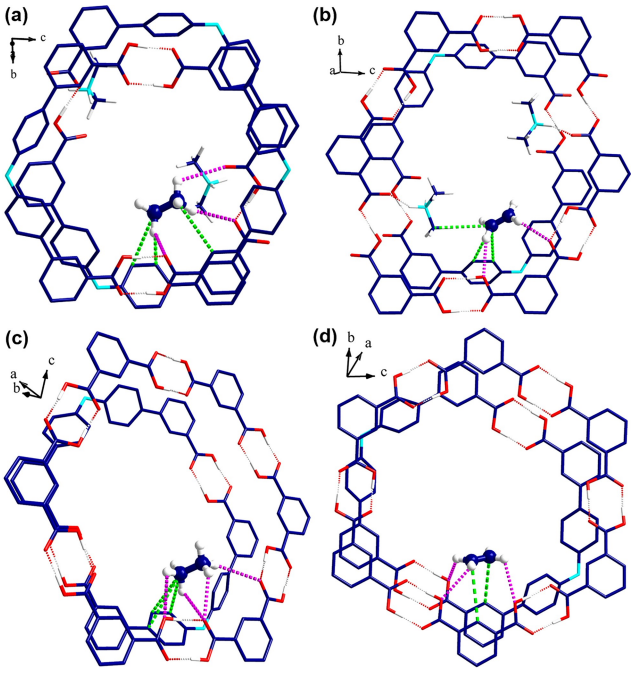


***Figure 7.*** Schematic theoretical calculated adsorption sites for (a) $C_2H_6$ and (b) $C_2H_4$ in **HOF-NBDA(DMA)**. The theoretical calculated adsorption sites for (c) $C_2H_6$ and (d) $C_2H_4$ in **HOF-NBDA**. The hydrogen atoms on the skeleton are omitted for clarity. The C–H···O interactions are shown in dashed purple lines and the C···C separations between gas molecule and the pore surface are shown in dashed green lines.

molecules are calculated as 35.8 and 31.0 kJ mol$^{-1}$. The difference in static binding energies of **HOF-NBDA** is 4.8 kJ mol$^{-1}$, which is higher than that in **HOF-NBDA-(DMA)**. The results of the theoretical calculation agree with the experimental isosteric heats ($Q_{st}$), which further proves that compared with **HOF-NBDA(DMA)**, **HOF-NBDA** with nonpolar pore surfaces possesses high ethane adsorption and separation performance.

## Conclusion

In conclusion, we have successfully tuned the pore polarization through in situ solid-state structural transformation between **HOF-NBDA(DMA)** and **HOF-NBDA**. Featuring larger and nonpolar pores, **HOF-NBDA** shows a dramatically enhanced performance on $C_2H_6$-selective adsorption compared with **HOF-NBDA(DMA)**. For **HOF-NBDA**, the difference in adsorption capacities for $C_2H_6$ and $C_2H_4$ is 23.4 cm$^3$ g$^{-1}$, and the $C_2H_6/C_2H_4$ uptake ratio is 136 %, which are significantly improved (For **HOF-NBDA(DMA)**, 5.0 cm$^3$ g$^{-1}$ and 108 % respectively). The experimental breakthrough curves confirmed that **HOF-NBDA** can efficiently adsorb $C_2H_6$ from $C_2H_6/C_2H_4$ (1/99, v/v) mixture to straightforwardly produce high-purity $C_2H_4$ with a significant interval of ca. 15.5 min g$^{-1}$, which is about a four-fold increase over **HOF-NBDA(DMA)**. The production of polymer-grade $C_2H_4$ produced by **HOF-NBDA** is 29.2 L kg$^{-1}$, which is much higher than that of **HOF-NBDA-(DMA)** (5.4 L kg$^{-1}$). The effective $C_2H_6/C_2H_4$ separation can also realize under different gas flow rates and temperatures on the **HOF-NBDA** packed column. In addition, in situ breakthrough experiments indicate the $C_2H_6/C_2H_4$ separation performance is greatly improved accompanied with the gradual heat treatment. Finally, theoretical calculations indicated that the pore surface of **HOF-NBDA** is enriched with $C_2H_6$-affinity sites, which can enhance the preferential binding of $C_2H_6$ over $C_2H_4$ and thus boost selective separation of $C_2H_6/C_2H_4$. These findings should inspire extensive research on new kind of $C_2H_6$-selective HOF materials for one-step $C_2H_6/C_2H_4$ separation.

## Acknowledgements

This work was supported by NSFC (21871266 and 22271282), Youth Innovation Promotion Association CAS and NSF of Fujian Province (No. 2021J01517 and 2020J06034).

## Conflict of Interest

The authors declare no competing financial interest.

## Data Availability Statement

The data that support the findings of this study are available in the Supporting Information of this article.

**Keywords:** $C_2H_6/C_2H_4$ Separation · Hydrogen-Bonded Organic Framework · Reticular Chemistry · Reverse-Order Adsorption · Solid Transformation

[1] D. S. Sholl, R. P. Lively, *Nature* **2016**, *532*, 435–437.
[2] R. Krishna, *ACS Omega* **2020**, *5*, 16987–17004.
[3] O. T. Qazvini, R. Babarao, Z.-L. Shi, Y.-B. Zhang, S. G. Telfer, *J. Am. Chem. Soc.* **2019**, *141*, 5014–5020.
[4] R.-B. Lin, H. Wu, L. Li, X.-L. Tang, Z. Li, J. Gao, H. Cui, W. Zhou, B. Chen, *J. Am. Chem. Soc.* **2018**, *140*, 12940–12946.
[5] P.-Q. Liao, W.-X. Zhang, J.-P. Zhang, X.-M. Chen, *Nat. Commun.* **2015**, *6*, 8697.
[6] L. Li, R.-B. Lin, R. Krishna, H. Li, S. Xiang, H. Wu, J. Li, W. Zhou, B. Chen, *Science* **2018**, *362*, 443–446.
[7] Y. Wang, C. Hao, W. Fan, M. Fu, X. Wang, Z. Wang, L. Zhu, Y. Li, X. Lu, F. Dai, Z. Kang, R. Wang, W. Guo, S. Hu, D. Sun, *Angew. Chem. Int. Ed.* **2021**, *60*, 11350–11358.
[8] Y. Wang, M. Fu, S. Zhou, H. Liu, X. Wang, W. Fan, Z. Liu, Z. Wang, D. Li, H. Hao, X. Lu, S. Hu, D. Sun, *Chem* **2022**, *8*, 3263–3274.
[9] Q. Dong, Y. Huang, K. Hyeon-Deuk, I. Y. Chang, J. Wan, C. Chen, J. Duan, W. Jin, S. Kitagawa, *Adv. Funct. Mater.* **2022**, *32*, 2203745.
[10] K.-J. Chen, D. G. Madden, S. Mukherjee, T. Pham, K. A. Forrest, A. Kumar, B. Space, J. Kong, Q.-Y. Zhang, M. J. Zaworotko, *Science* **2019**, *366*, 241–246.

[11] B. Zhu, J.-W. Cao, S. Mukherjee, T. Pham, T. Zhang, T. Wang, X. Jiang, K. A. Forrest, M. J. Zaworotko, K.-J. Chen, *J. Am. Chem. Soc.* **2021**, *143*, 1485–1492.
[12] X. Zhang, L. Li, J.-X. Wang, H.-M. Wen, R. Krishna, H. Wu, W. Zhou, Z.-N. Chen, B. Li, G. Qian, B. Chen, *J. Am. Chem. Soc.* **2020**, *142*, 633–640.
[13] L. Yang, L. Yan, W. Niu, Y. Feng, Q. Fu, S. Zhang, Y. Zhang, L. Li, X. Gu, P. Dai, D. Liu, Q. Zheng, X. Zhao, *Angew. Chem. Int. Ed.* **2022**, *61*, e202204046.
[14] S.-M. Wang, H.-R. Liu, S.-T. Zheng, H.-L. Lan, Q.-Y. Yang, Y.-Z. Zheng, *Sep. Purif. Technol.* **2023**, *304*, 122378.
[15] G.-D. Wang, J. Chen, Y.-Z. Li, L. Hou, Y.-Y. Wang, Z. Zhu, *Chem. Eng. J.* **2022**, *433*, 133786.
[16] J. Pei, J.-X. Wang, K. Shao, Y. Yang, Y. Cui, H. Wu, W. Zhou, B. Li, G. Qian, *J. Mater. Chem. A* **2020**, *8*, 3613–3620.
[17] S. Geng, E. Lin, X. Li, W. Liu, T. Wang, Z. Wang, D. Sensharma, S. Darwish, Y. H. Andaloussi, T. Pham, P. Cheng, M. J. Zaworotko, Y. Chen, Z. Zhang, *J. Am. Chem. Soc.* **2021**, *143*, 8654–8660.
[18] Z. Di, C. Liu, J. Pang, S. Zou, Z. Ji, F. Hu, C. Chen, D. Yuan, M. Hong, M. Wu, *Angew. Chem. Int. Ed.* **2022**, *61*, e202210343.
[19] X. Zhang, J.-X. Wang, L. Li, J. Pei, R. Krishna, H. Wu, W. Zhou, G. Qian, B. Chen, B. Li, *Angew. Chem. Int. Ed.* **2021**, *60*, 10304–10310.
[20] J.-X. Wang, X.-W. Gu, Y.-X. Lin, B. Li, G. Qian, *ACS Mater. Lett.* **2021**, *3*, 497–503.
[21] J. Liu, J. Miao, S. Ullah, K. Zhou, L. Yu, H. Wang, Y. Wang, T. Thonhauser, J. Li, *ACS Mater. Lett.* **2022**, *4*, 1227–1232.
[22] Y.-L. Li, E. V. Alexandrov, Q. Yin, L. Li, Z.-B. Fang, W. Yuan, D. M. Proserpio, T.-F. Liu, *J. Am. Chem. Soc.* **2020**, *142*, 7218–7224.
[23] B. Yu, S. Geng, H. Wang, W. Zhou, Z. Zhang, B. Chen, J. Jiang, *Angew. Chem. Int. Ed.* **2021**, *60*, 25942–25948.
[24] X. Ding, Z. Liu, Y. Zhang, G. Ye, J. Jia, J. Chen, *Angew. Chem. Int. Ed.* **2022**, *61*, e202116483.
[25] J. Gao, Y. Cai, X. Qian, P. Liu, H. Wu, W. Zhou, D.-X. Liu, L. Li, R.-B. Lin, B. Chen, *Angew. Chem. Int. Ed.* **2021**, *60*, 20400–20406.
[26] R.-B. Lin, Y. He, P. Li, H. Wang, W. Zhou, B. Chen, *Chem. Soc. Rev.* **2019**, *48*, 1362–1389.
[27] J.-R. Li, R. J. Kuppler, H.-C. Zhou, *Chem. Soc. Rev.* **2009**, *38*, 1477–1504.
[28] O. M. Yaghi, *ACS Cent. Sci.* **2019**, *5*, 1295–1300.
[29] W. Lu, Z. Wei, Z.-Y. Gu, T.-F. Liu, J. Park, J. Park, J. Tian, M. Zhang, Q. Zhang, T. Gentle III, M. Bosch, H.-C. Zhou, *Chem. Soc. Rev.* **2014**, *43*, 5561–5593.
[30] R. Freund, S. Canossa, S. M. Cohen, W. Yan, H. Deng, V. Guillerm, M. Eddaoudi, D. G. Madden, D. Fairen-Jimenez, H. Lyu, L. K. Macreadie, Z. Ji, Y. Zhang, B. Wang, F. Haase, C. Woell, O. Zaremba, J. Andreo, S. Wuttke, C. S. Diercks, *Angew. Chem. Int. Ed.* **2021**, *60*, 23946–23974.
[31] H. Jiang, D. Alezi, M. Eddaoudi, *Nat. Rev. Mater.* **2021**, *6*, 466–487.
[32] Y. Yang, H. Zhang, Z. Yuan, J.-Q. Wang, F. Xiang, L. Chen, F. Wei, S. Xiang, B. Chen, Z. Zhang, *Angew. Chem. Int. Ed.* **2022**, *61*, e202207579.
[33] Y. Yang, L. Li, R.-B. Lin, Y. Ye, Z. Yao, L. Yang, F. Xiang, S. Chen, Z. Zhang, S. Xiang, B. Chen, *Nat. Chem.* **2021**, *13*, 933–939.
[34] L. Wang, L. Yang, L. Gong, R. Krishna, Z. Gao, Y. Tao, W. Yin, Z. Xu, F. Luo, *Chem. Eng. J.* **2020**, *383*, 123117.
[35] H. Wang, B. Li, H. Wu, T.-L. Hu, Z. Yao, W. Zhou, S. Xiang, B. Chen, *J. Am. Chem. Soc.* **2015**, *137*, 9963–9970.
[36] J. Liang, S. Xing, P. Brandt, A. Nuhnen, C. Schluesener, Y. Sun, C. Janiak, *J. Mater. Chem. A* **2020**, *8*, 19799–19804.
[37] P. Li, Y. He, H. D. Arman, R. Krishna, H. Wang, L. Weng, B. Chen, *Chem. Commun.* **2014**, *50*, 13081–13084.
[38] B. Wang, R.-B. Lin, Z. Zhang, S. Xiang, B. Chen, *J. Am. Chem. Soc.* **2020**, *142*, 14399–14416.
[39] K. Sarkar, P. Dastidar, *Langmuir* **2018**, *34*, 685–692.
[40] C. H. Lui, L. Liu, K. F. Mak, G. W. Flynn, T. F. Heinz, *Nature* **2009**, *462*, 339–341.
[41] H. Fang, B. Zheng, Z.-H. Zhang, P.-B. Jin, H.-X. Li, Y.-Z. Zheng, D.-X. Xue, *ACS Appl. Mater. Interfaces* **2022**, *14*, 44460–44469.
[42] A. L. Spek, *Acta Crystallogr. Sect. E* **2020**, *76*, 1–11.
[43] T.-U. Yoon, S. B. Baek, D. Kim, E.-J. Kim, W.-G. Lee, B. K. Singh, M. S. Lah, Y.-S. Bae, K. S. Kim, *Chem. Commun.* **2018**, *54*, 9360–9363.
[44] M. Nishio, *CrystEngComm* **2004**, *6*, 130–158.
[45] D. Z. Veljkovic, G. V. Janjic, S. D. Zaric, *CrystEngComm* **2011**, *13*, 5005–5010.
[46] G. R. Desiraju, *Chem. Commun.* **2005**, 2995–3001.
[47] Deposition numbers 2235806 (for **HOF-NBDA(DMA)**) and 2235816 (for **HOF-NBDA**) contain the supplementary crystallographic data for this paper. These data are provided free of charge by the joint Cambridge Crystallographic Data Centre and Fachinformationszentrum Karlsruhe Access Structures service.

Manuscript received: April 10, 2023
Accepted manuscript online: April 26, 2023
Version of record online: May 10, 2023

Angewandte Chemie
Eine Zeitschrift der Gesellschaft Deutscher Chemiker

Supporting Information

# Tuning Pore Polarization to Boost Ethane/Ethylene Separation Performance in Hydrogen-Bonded Organic Frameworks

*Y. Zhou, C. Chen, R. Krishna, Z. Ji, D. Yuan, M. Wu**

## Materials and Instrumentation:

Unless otherwise stated, all reagents and solvents used in studies were purchased from commercial sources and were used without further purification.

$^1$H NMR spectra were obtained on a Bruker AVANCE III 400 (400 MHz) spectrometers. Crystallographical data were collected on a XtaLAB Synergy R, HyPix diffractometer equipped with Cu Kα radiation (λ = 1.54184 Å). Powder X-ray diffraction (PXRD) patterns were performed on a MiniFlex 600 diffractometer equipped using Cu Kα (λ = 1.5406 Å), scanning at 1°/ min in a range of 4~50°. In order to collect the PXRD patterns at different temperatures, the sample was heated in air to the anticipated temperature and maintained for 10 min. The thermogravimetric analysis (TGA) was performed on a NETZSCH STA 449C unit at a heating rate of 10 ℃·min$^{-1}$ under nitrogen atmosphere. The morphology of HOF-NBDA was characterized by using scanning electron microscopy ZEISS SIGMA 300 microscope.

## Experimental Section:

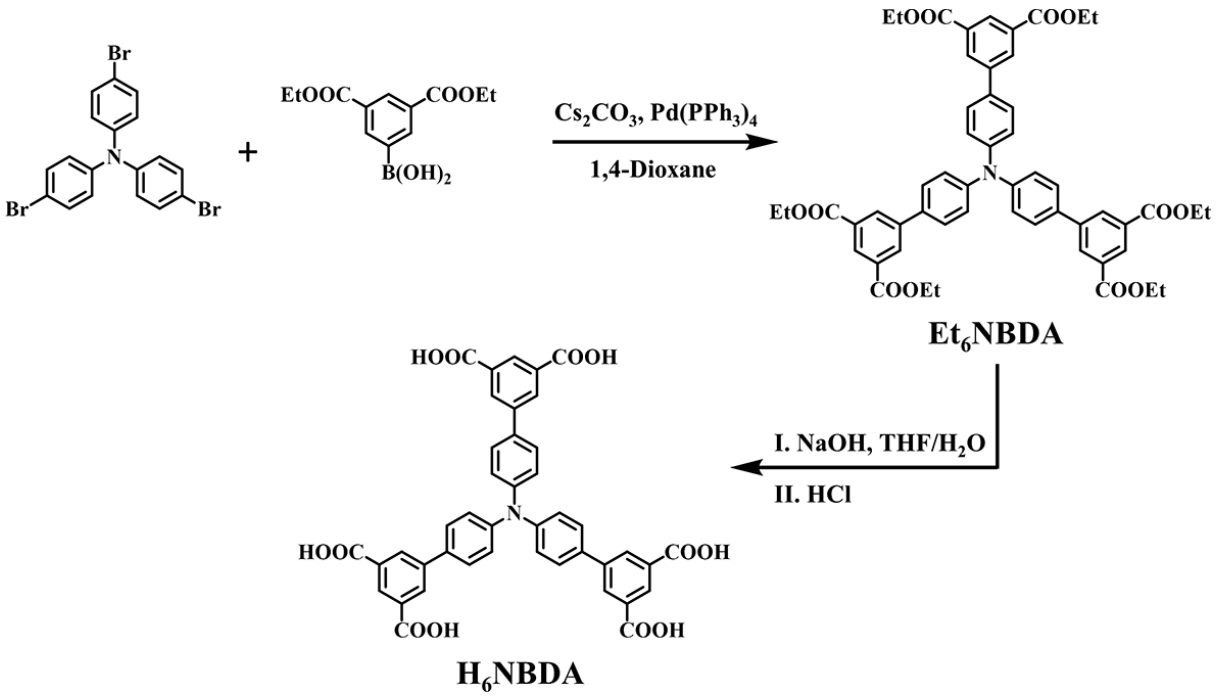


**Scheme S1.** Synthesis routine of the $H_6$NBDA ligand.

## Synthesis of $Et_6$NBDA

The organic compound $Et_6$NBDA was synthesized by using the Suzuki-Miyaura coupling reaction. A mixture of tris(4-bromophenyl)-amine (1.5 g, 3.0 mmol), (3,5-bis(ethoxycarbonyl)phenyl)-boronic acid (5.2 g, 15.0 mmol), $Cs_2CO_3$ (6.5 g, 20.0 mmol) and $Pd(PPh_3)_4$ (0.2 g, 0.2 mmol) were dissolved in 250 mL degassed 1,4-dioxane

solvent, and then heated at 85 °C for 72 h under $N_2$ atmosphere. After the reaction was completed and cooled to room temperature, the organic solvent was removed under vacuum. 200 mL deionized water was added to the concentrated mixture, followed by extraction with dichloromethane (3 × 50 mL), and the combined extraction was dried with anhydrous $Mg_2SO_4$. After filtration, the dichloromethane was removed under vacuum, and then the crude product was purified by silica gel column chromatography to give 2.3 g yellow powdery solid $Et_6$NBDA (yield: 85 %). $^1$H NMR (400 MHz, $CDCl_3$): *δ*, 1.31 (t, 18H), 4.47 (q, 12H), 7.31 (d, 6H), 7.65 (d, 6H), 8.49 (s, 6H), 8.66 (s, 3H).

## Synthesis of $H_6$NBDA

The purified intermediate $Et_6$NBDA (5.0 g, 5.5 mmol) was dissolved in THF (200 mL), and 100 mL of KOH aqueous solution (4.5 M) was added. The resulting mixture was heated at 85 °C to stir and refluxed for 12 h. The volatiles were removed in vacuum, and then 250 mL deionized water was added to give a bright yellow clear solution. Then the solvent pH value was adjusted to 1 with concentrated hydrochloric acid. The resulting yellow solid was collected by filtration and washed several times with deionized water until neutral. After drying, yellow compound 3.7 g was obtained (yield: 90 %). $^1$H NMR (400 MHz, DMSO-$d_6$) (Figure S1): *δ*, 7.26 (d, 6H), 7.78 (d, 6H), 8.41 (t, 9H), 13.42 (s, 6H).

## Synthesis of HOF-NBDA(DMA)

$H_6$NBDA (120 mg, 0.2 mmol) was added to 3 mL DMF in a 25 mL Teflon vessel of the hydrothermal bomb and sonicated for 5 minutes. Then 60 μL glacial acetic acid was added to the mixture. The vessel was heated at 120 °C for two days and then slowly cooled to room temperature within one day. The yellow bulk crystals HOF-NBDA(DMA) ($[(Me_2NH_2)_2(H_5NBDA)_2]_n$) suitable for single crystal X-ray diffraction were obtained (80 mg, yield 66.7 %). $^1$H NMR (400 MHz, DMSO-$d_6$): *δ*, 2.57 (s, 6H), 7.25 (d, 6H), 7.75 (d, 6H), 8.42 (t, 9H), 13.42 (s, 6H).

## Synthesis of HOF-NBDA

The HOF-NBDA(DMA) crystals were exchanged with dry methanol for 3 days by replacing fresh methanol every 6 hours at room temperature. Then, the samples were degassed under dynamic vacuum at 100 °C for 10 h to afford HOF-NBDA, which can be demonstrated by PXRD patterns and $^1$H NMR spectrum (Figure S1). Though the crystals break into pieces, fortunately the tiny crystals are suitable for single crystal X-ray diffraction. $^1$H NMR (400 MHz, DMSO-$d_6$): *δ*, 7.26 (d, 6H), 7.78 (d, 6H), 8.40 (t, 9H), 13.42 (s, 6H).

## Scale-up synthesis of HOF-NBDA

In order to obtain a good deal of sample in one batch for adsorption and separation experiments, $H_6$NBDA (10.0 g, 13.5 mmol) was dissolved in 150 mL dry DMF in a beaker and the mixture was filtrated by a filter membrane (50 mm, 0.22 μm). Then 500 mL dry methanol was slowly added to the mixture with stirring, and yellow crystals were rapidly precipitated. The products were separated by suction filtration and further washed several times with methanol, which can be characterized by PXRD patterns and $^1$H NMR spectrum. $^1$H NMR (400 MHz, DMSO-$d_6$): *δ*, 7.26 (d, 6H), 7.78 (d, 6H), 8.42 (t, 9H), 13.43 (s, 6H).

## Single-Crystal X-ray Crystallography

The X-ray diffraction data for HOF-NBDA(DMA) and HOF-NBDA were performed on a XtaLAB Synergy R, HyPix diffractometer with Cu Kα radiation at 150K (λ = 1.54184 Å). Absorption corrections were performed using a multi-scan method. The structures were solved by direct methods and were refined by the least-squares method with *SHELXL*-2018 program package. All non-hydrogen atoms were refined with anisotropic displacement parameters. Hydrogen atoms of the ligands were located by geometrical calculations, and their positions and thermal parameters were fixed during structural refinement. We use the "squeeze" command of the *PLATON* to clear the above-mentioned residual electron-density peaks to improve the quality of crystal structure data.

## Adsorption/desorption experiments

All gas adsorption measurements were measured on Micromeritics 3 Flex. All the sorption experiments were maintained at 77 K with liquid nitrogen, at 273 K in an ice-water bath and 298 K in a water bath. The fresh sample of HOF-NBDA(DMA) was exchanged with dry methanol for 7 days and then the supercritical carbon dioxide (sc-$CO_2$) drying was used to obtain guest-free HOF-NBDA(DMA) with sc-$CO_2$ in a Tousimis™ Samdri® PVT-3D critical point dryer. After sc-$CO_2$ treatment, guest-free HOF-NBDA(DMA) was tranfered to Micromeritics 3 Flex to carry out the experiment. In order to investigate the solid transformation of HOF-NBDA(DMA) into HOF-NBDA, guest-free HOF-NBDA(DMA) with sc-$CO_2$ was heated at 100 °C for 10 hours under a high vacuum to obtain HOF-NBDA. For HOF-NBDA, the scale-up synthesis sample was exchanged with dry methanol for 7 days and then vacuumed at room temperature for 12 hours. The above sample was then heated at 100 °C for 10 hours under a high vacuum. Then, guest-free HOF-NBDA was tranfered to Micromeritics 3 Flex to carry out the experiment.

## Fitting of unary isotherm data

The unary isotherms for $C_2H_6$ and $C_2H_4$ measured at different temperatures in HOF-NBDA(DMA) and HOF-NBDA were fitted with excellent accuracy using either the 1-site Langmuir-Freundlich model:

$$q = \frac{q_{sat} b p^{v}}{1 + b p^{v}} \tag{S1}$$

In eq (S1), the Langmuir-Freundlich parameter $b$ is temperature dependent,

$$b = b_0 \exp\left(\frac{E}{RT}\right) \tag{S2}$$

In eq (S2), $E$ is the energy parameter.

The unary isotherm fit parameters for HOF-NBDA and HOF-NBDA(DMA) are provided in Table S1 and Table S2.

**Table S1.** 1-site Langmuir-Freundlich parameter fits for $C_2H_6$ and $C_2H_4$ in HOF-NBDA.

| | $q_{sat}$ (mol·kg$^{-1}$) | $b_0$ (Pa$^{-v}$) | E (kJ·mol$^{-1}$) | $v$ |
|---|---|---|---|---|
| $C_2H_6$ | 6.8 | 3.636E-11 | 27.3 | 1.16 |
| $C_2H_4$ | 8.25 | 1.409E-10 | 22.5 | 1.13 |

**Table S2**. 1-site Langmuir-Freundlich parameter fits for $C_2H_6$ and $C_2H_4$ in HOF-NBDA(DMA).

| | $q_{sat}$ (mol·kg$^{-1}$) | $b_0$ (Pa$^{-v}$) | E (kJ·mol$^{-1}$) | $v$ |
|---|---|---|---|---|
| $C_2H_6$ | 4.15 | 8.794E-11 | 28.5 | 1.09 |
| $C_2H_4$ | 4.25 | 1.287E-10 | 26.3 | 1.1 |

## Isosteric heat of adsorption

The isosteric heat of adsorption, $Q_{st}$, is defined as

$$Q_{st} = -RT^2 \left(\frac{\partial \ln p}{\partial T}\right)_q \tag{S3}$$

where the derivative in the right member of eq (S3) is determined at constant adsorbate loading, $q$. The derivative was determined by analytic differentiation of the combination of eq (S1), eq (S2), and eq (S3).

## Separation potential

$C_2H_6(1)/C_2H_4(2)$ mixture separations are envisaged to be carried out in fixed bed adsorbers. In such devices, the separations are dictated by a combination of adsorption selectivity and uptake capacity. Using the shock wave

model for fixed bed adsorbers, Krishna[1-2] has suggested that the appropriate metric is the separation potential, $\Delta q_1$.

$$\Delta q = q_1 \frac{y_{20}}{y_{10}} - q_2 \tag{S4}$$

In eq (S4) $y_{10}$, $y_{20}$ are the mole fractions of the feed mixture during the adsorption cycle. In the derivation of eq (S4), it is assumed that the concentration "fronts" traversed the column in the form of shock waves during the desorption cycle. The molar loadings $q_1$, $q_2$ of the two components are determined using the Ideal Adsorbed Solution Theory (IAST) of Myers and Prausnitz using the unary isotherm fits as data inputs.[3] The physical significance of $\Delta q$ is the maximum productivity of pure $C_2H_4$(2) that is achievable in the adsorption cycle of PSA operations.

## Transient breakthrough experiments vs simulations

Transient breakthrough experiments were carried out for binary 1/99 $C_2H_6$(1)/$C_2H_4$(2) mixtures at a total pressure of 0.15 MPa and 298 K. The sample mass of HOF in the packed bed, $m_{ads}$ is 1.4 g. The flow rates at the inlet, $Q_0$ = 2 mL min$^{-1}$. Transient breakthrough simulations were carried out for the exact same set of operating conditions as in the experiments, using the methodology described in earlier publications.[1-2, 4-6] In these simulations, intra-crystalline diffusion influences are ignored. There is very good match between the experiments and simulations. From the transient breakthrough simulations, it is established that polymer grade $C_2H_4$ is recoverable. The productivities of purified $C_2H_4$ are determined as follows.

| $C_2H_4$ product purity | $C_2H_4$ productivity |
|---|---|
| 99.95%+ | 1.39 mol·kg$^{-1}$ (31.1 L·kg$^{-1}$) |
| 99.9%+ | 1.6 mol·kg$^{-1}$ |

For 1/15 $C_2H_6$(1)/$C_2H_4$(2) mixtures the sample mass of HOF in the packed bed, $m_{ads}$ is 1.7 g, The transient breakthrough simulations yielded the productivities of purified $C_2H_4$ as follows.

| $C_2H_4$ product purity | $C_2H_4$ productivity |
|---|---|
| 99.95%+ | 1.00 mol·kg$^{-1}$ |
| 99.9%+ | 1.11 mol·kg$^{-1}$ |

For 1/9 $C_2H_6$(1)/$C_2H_4$(2) mixtures the sample mass of HOF in the packed bed, $m_{ads}$ is 1.7 g, The transient breakthrough simulations yielded the productivities of purified $C_2H_4$ as follows.

| $C_2H_4$ product purity | $C_2H_4$ productivity |
|---|---|
| 99.95%+ | 0.9 mol·kg$^{-1}$ |
| 99.9%+ | 1.03 mol·kg$^{-1}$ |

## Column breakthrough experiments

The breakthrough separation experiments for $C_2H_6$/$C_2H_4$ (1/99, v/v) were conducted in a fixed bed under ambient conditions. A quartz column with a length of 500 mm and an inner diameter of 3 mm was used for sample packing. The flow rate of the gas was regulated by a mass flow controller, and the gas flow out of the chromatographic column was detected by a gas chromatography (GC) with FID detector. All measurements were performed following a protocol established by the literature. In a vacuum glove box, 1.84 g HOF-NBDA(DMA) activated by sc-$CO_2$ was quickly loaded into a quartz column. After each separation experiment, the sample was *in situ* blowed with a He flow (20 mL·min$^{-1}$) for 4.0 h at a given temperature. For HOF-NBDA, in a vacuum glove box, 1.40 g sample was loaded into a quartz column. After each separation experiment, the HOF-NBDA sample was blowed under He flow (20 mL·min$^{-1}$) for 2.0 h at 373 K. For 1/9 and1/15 $C_2H_6$/$C_2H_4$ mixture, the sample mass of HOF-NBDA in the packed bed was 1.70 g, and other conditions being the same to the above experiment.

## Computational details

The binding sites for $C_2H_6$ and $C_2H_4$ in HOF-NBDA(DMA) and HOF-NBDA were determined through classical molecular simulations. The single X-ray crystallographic structures were subject to geometry optimization through the Dmol3 module implemented with the Materials Studio program, using the generalized gradient approximation (GGA) with the Perdew-Burke-Ernzerhof (PBE) functional and the double numerical plus d-functions (DNP) basis set. The energy, force, and displacement convergence criteria were set as $1 \times 10^{-5}$ Ha, $2 \times 10^{-3}$ Ha/Å and $5 \times 10^{-3}$ Å, respectively. The calculated electrostatic potential for HOF-NBDA(DMA) and HOF-NBDA was mapped onto the Connolly surface with a probe radius of 1.0 Å. Simulated annealing (SA) calculations were performed for a single molecule of $C_2H_6$ and $C_2H_4$ through a canonical Monte Carlo (NVT) process, and all HOF atoms were kept fixed at their positions throughout the simulations. The initial configurations were further optimized to ensure a more efficient energy landscape scanning for every HOF-$C_2H_x$ complex, and the optimized configuration having the lowest energy was used as the global minimum for the subsequent analysis and calculation. The static binding energy (at T= 0 K) was then calculated: $\triangle E = E_{HOF} + E_{gas} - E_{HOF+gas}$.

## Additional Data and Pictures

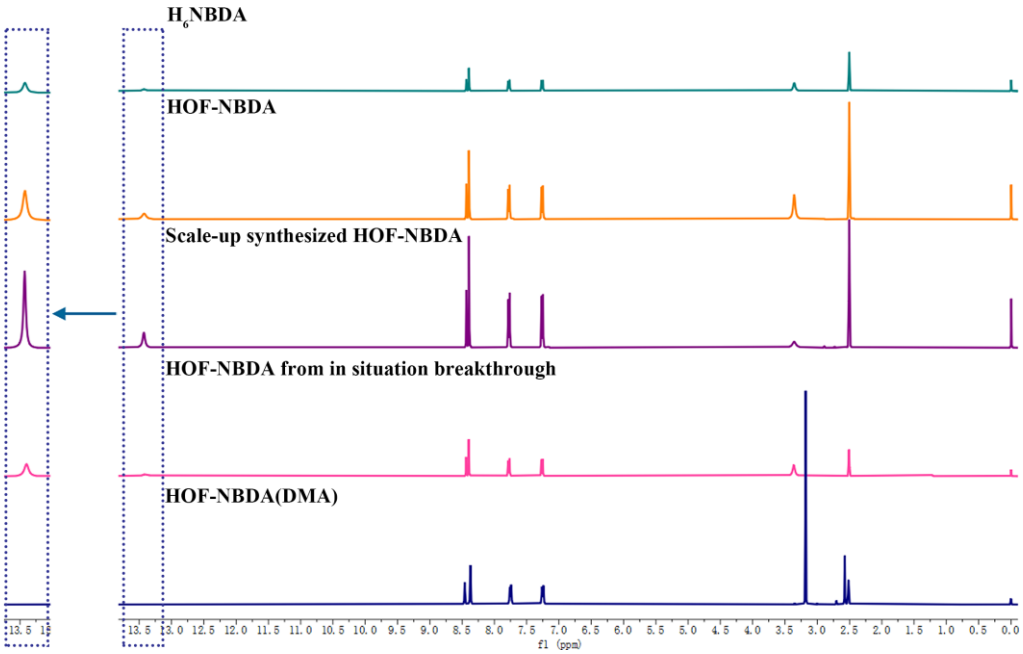


**Figure S1.** $^{1}$H NMR (DMSO-$d_6$, 400 MHz) spectrum of $H_6$NBDA, **HOF-NBDA**, scale-up synthesized **HOF-NBDA**, **HOF-NBDA** from in situation breakthrough and **HOF-NBDA(DMA)**.

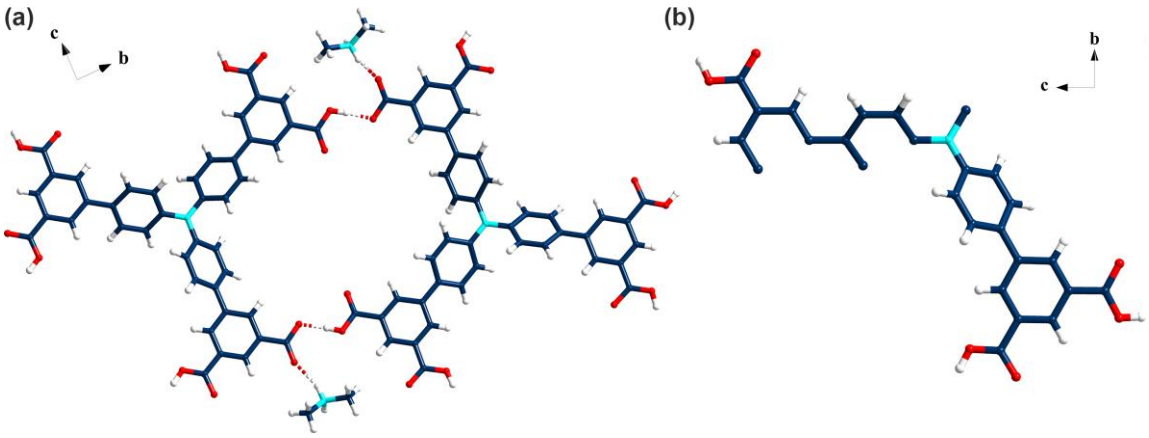


**Figure S2.** The asymmetric units of (a) **HOF-NBDA(DMA)** and (b) **HOF-NBDA**.

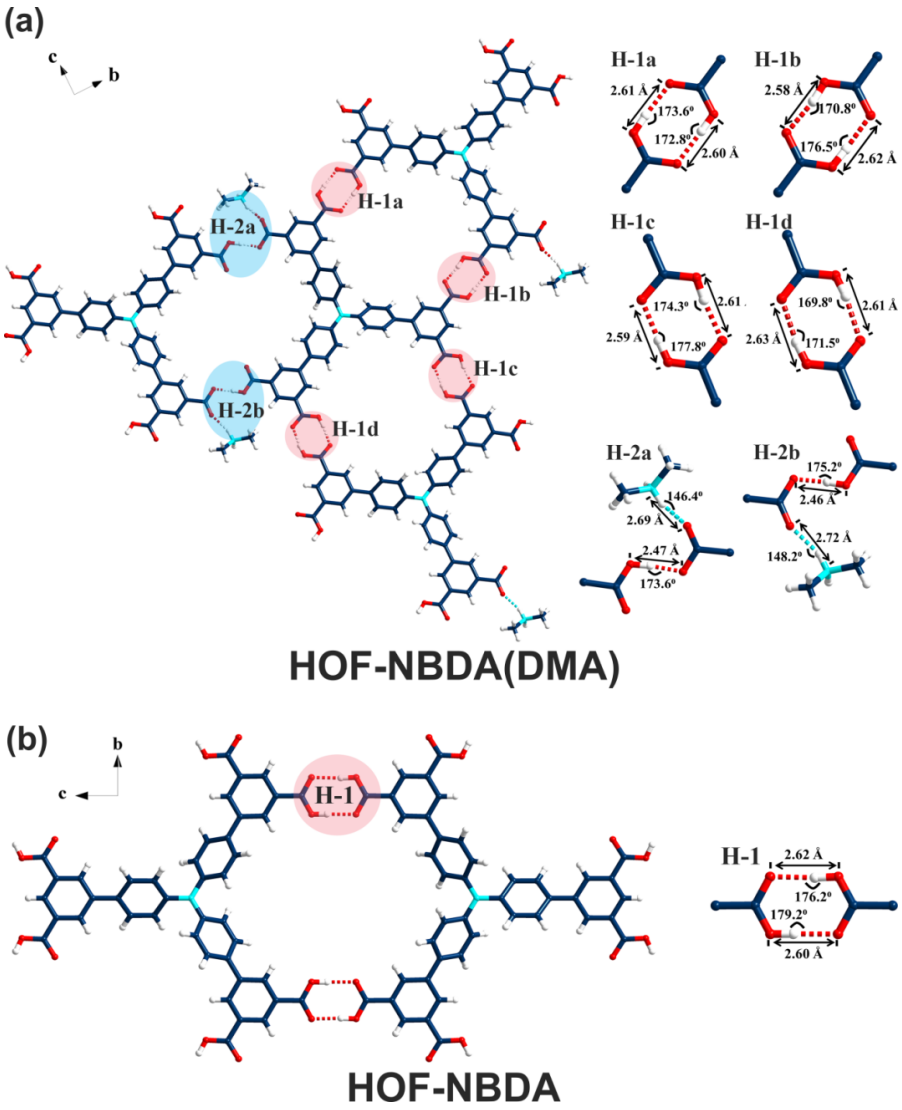


**Figure S3.** (a) $H_6$NBDA molecules are arranged to form four sets of carboxyl…carboxyl dimers (∠O–H···O ranging from 169.8° to 177.8°, d (O–H···O) ranging from 2.46 to 2.63 Å.) and two pairs of N–H···O hydrogen bonds (∠N–H···O recorded as 146.4° and 148.2°, *d* (N–H···O) recorded as 2.69 Å and 2.72 Å) in **HOF-NBDA(DMA)**. (b) The adjacent $H_6$NBDA molecules are interconnected through solo carboxyl…carboxyl dimers (∠O–H···O record as 179.2° and 176.2°, *d* (O–H···O) record as 2.60 and 2.62 Å, respectively.) in **HOF-NBDA**.

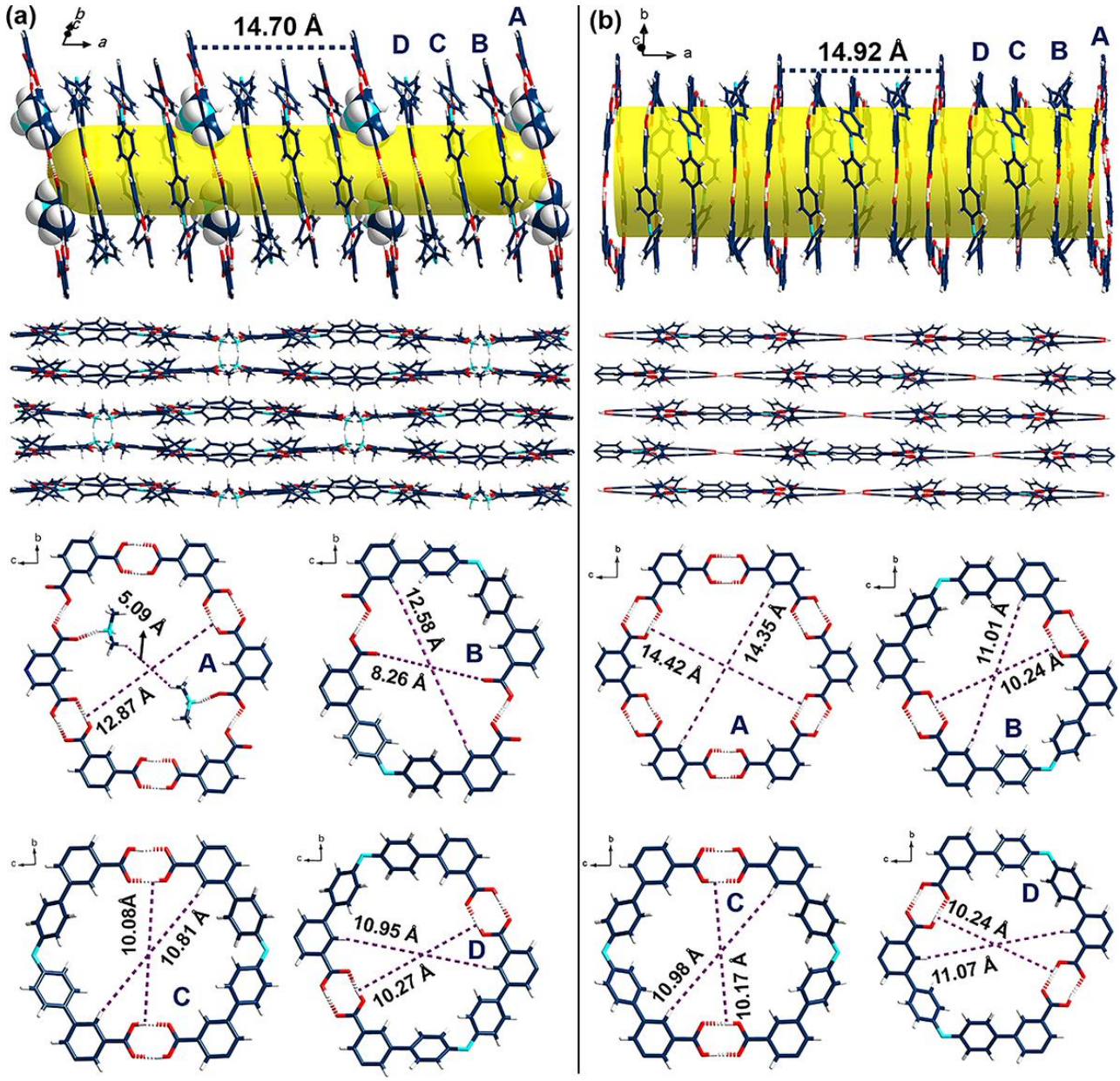


**Figure S4.** A cross-section view of the hexagonal porous windows in (a) **HOF-NBDA(DMA)** and (b) **HOF-NBDA**. The layered frameworks are stacked in slippage in a -ABCD- manner without interpenetration with average interlayer distances of ca. 3.68 and 3.73 Å, respectively. The porous window details of A, B, C and D layers with different pore sizes are described.

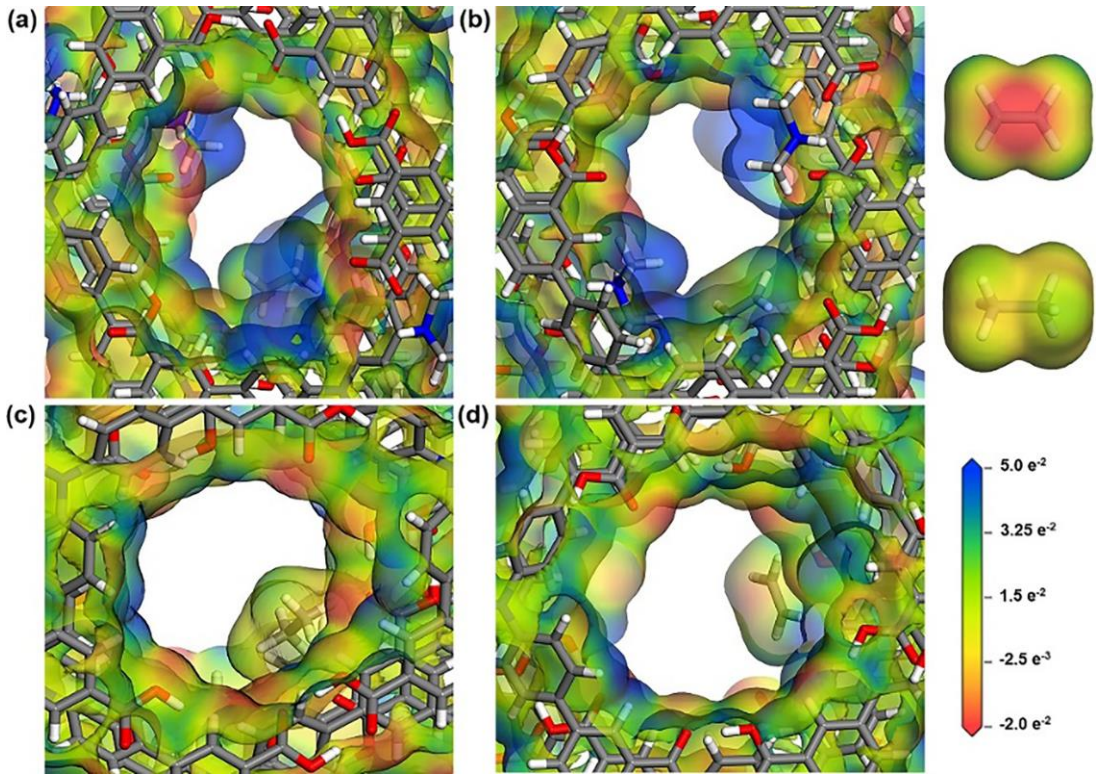


**Figure S5.** The changes of electrostatic potential (ESP) on the guests loaded pore walls, (a) **$C_2H_6$@HOF-NBDA(DMA)**, (b) **$C_2H_4$@HOF-NBDA(DMA)**, (c) **$C_2H_6$@HOF-NBDA** and (d) **$C_2H_4$@HOF-NBDA**, respectively. The gradation on the scale bar is in Hartree/e. The molecular electrostatic potential (MEP) of the $C_2H_4$ and $C_2H_6$ molecules mapped onto the Connolly surface.

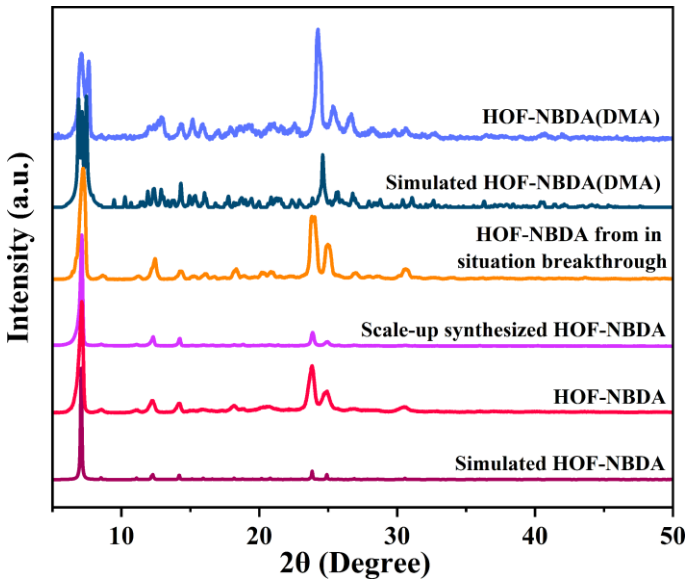


**Figure S6.** PXRD patterns of simulated **HOF-NBDA**, **HOF-NBDA**, the scale-up synthesized **HOF-NBDA**, **HOF-NBDA** from in situation breakthrough, simulated **HOF-NBDA(DMA)** and **HOF-NBDA(DMA)**.

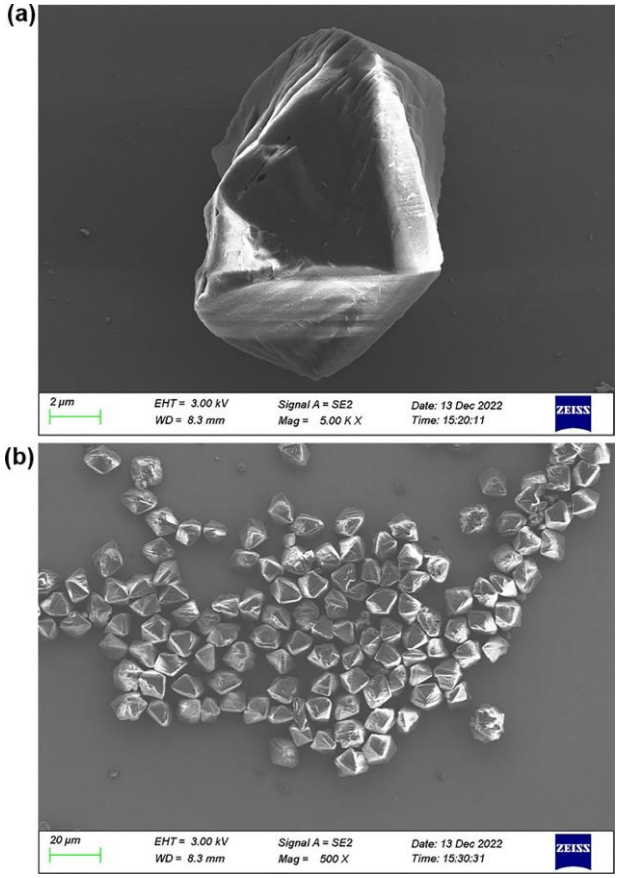


**Figure S7.** The scanning electron microscope photographs of the scale-up synthesized **HOF-NBDA** crystals.

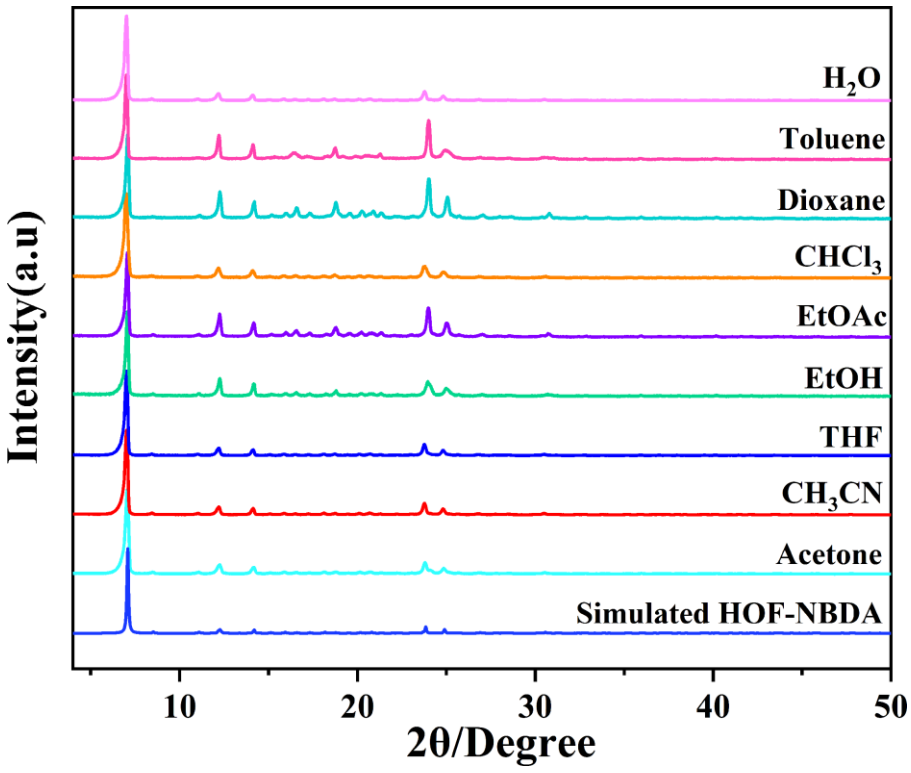


**Figure S8.** PXRD patterns of **HOF-NBDA** after treated with different solvents for one day.

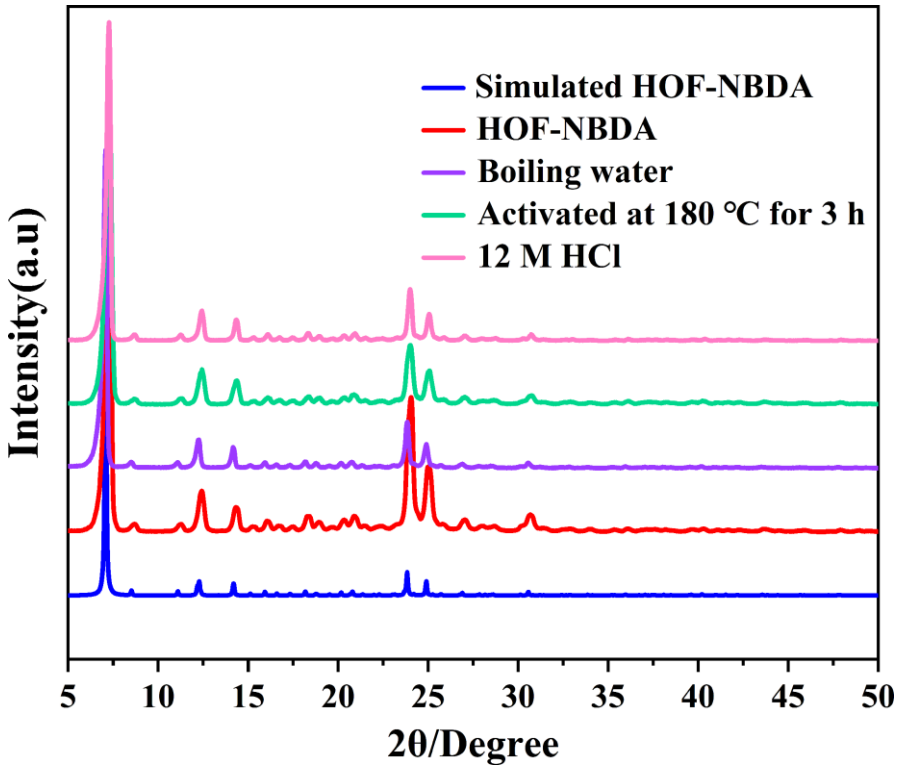


**Figure S9.** The PXRD patterns of **HOF-NBDA** are almost unchanged after heating at 180 °C in air atmosphere, and even soaking in boiling water or harsher chemical environment such as 12 M HCl for 24 h.

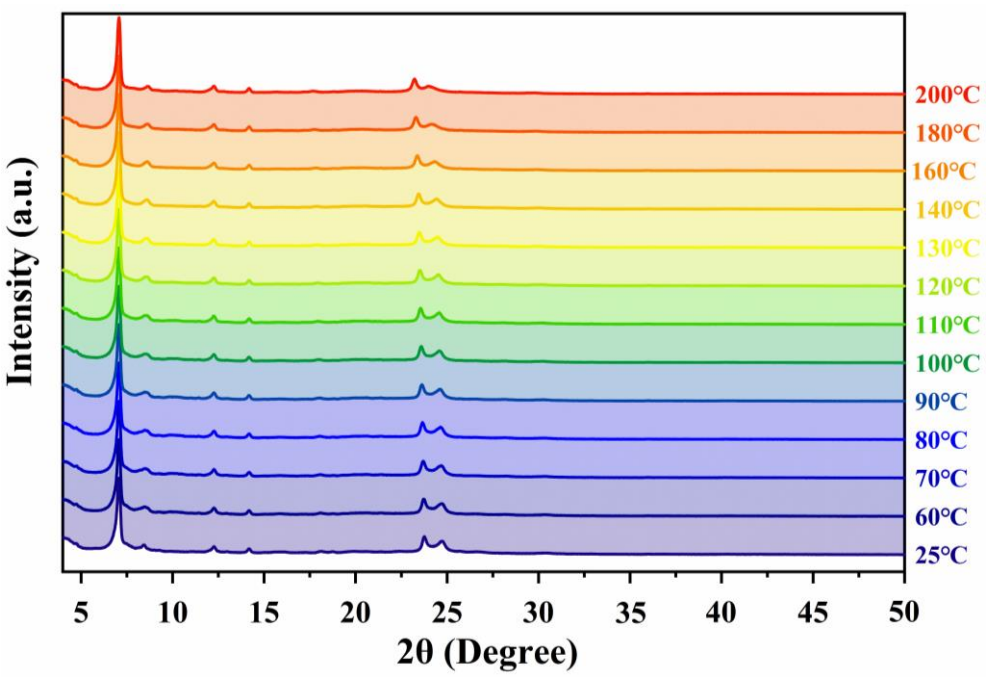


**Figure S10.** Variable-temperature PXRD patterns for **HOF-NBDA** in air atmosphere.

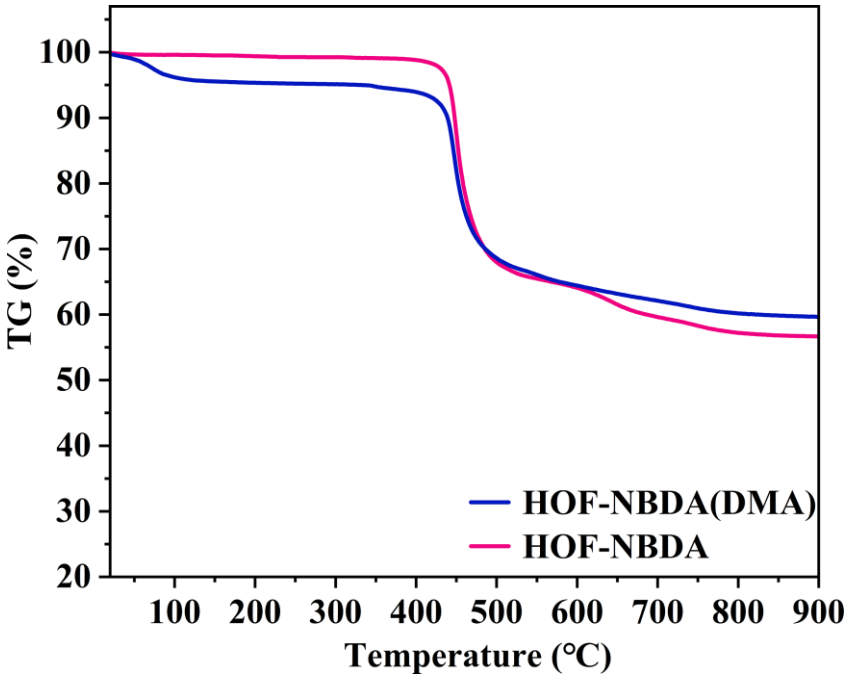


**Figure S11.** TGA curve of **HOF-NBDA(DMA)** (blue) and **HOF-NBDA** (red). The freshly synthesized **HOF-NBDA** experienced a weight loss before 100 °C, which was due to the removal of solvent molecules in the voids. The synthesized **HOF-NBDA(DMA)** experienced a weight loss before 200 °C, which was due to the removal of solvent molecules and the DMA molecules in the voids.

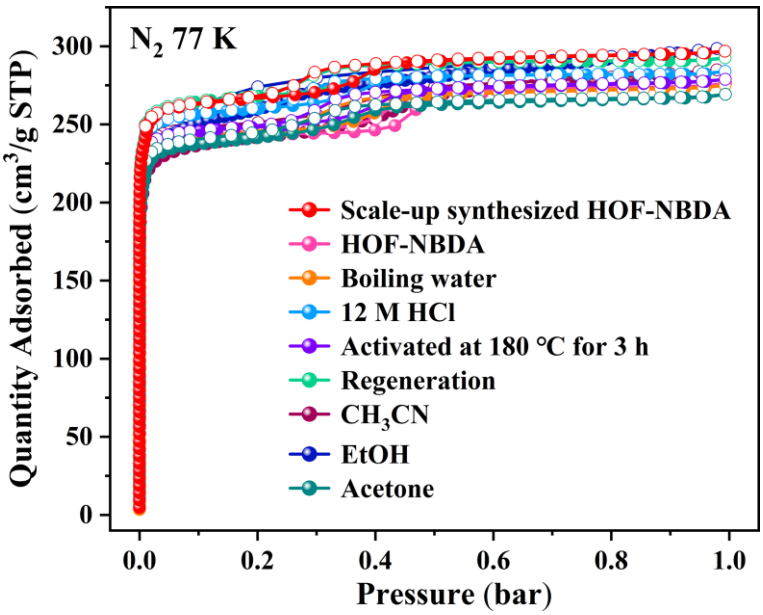


**Figure S12.** $N_2$ adsorption isotherms (77 K) of **HOF-NBDA** after treated under different conditions. In addition, the damaged samples can be easily reproduced by dissolving in DMF solution, and the $N_2$ uptake of recrystallized sample is almost the same as the original sample.

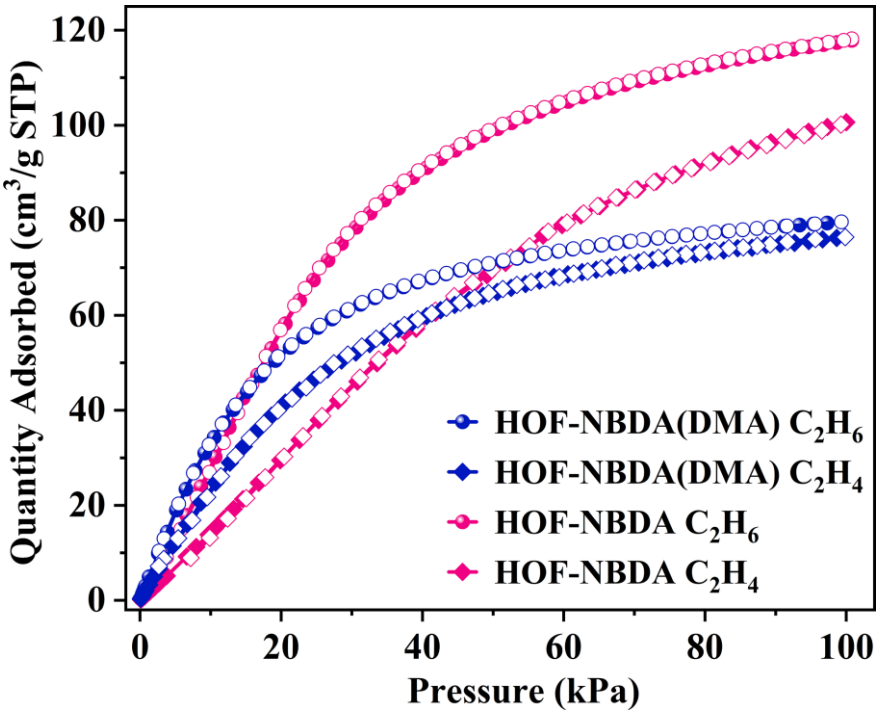


**Figure S13.** $C_2H_6$ and $C_2H_4$ adsorption isotherms of **HOF-NBDA(DMA)** (blue) and **HOF-NBDA** (red) at 273 K.

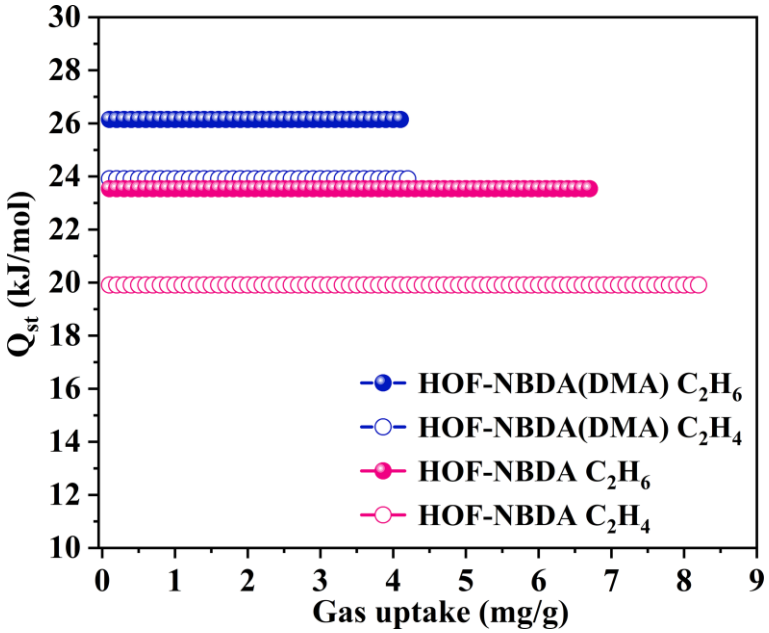


**Figure S14.** Calculated isosteric heats of adsorption of $C_2H_6$ and $C_2H_4$ in **HOF-NBDA** (red line) and **HOF-NBDA(DMA)** (blue line). The experimental isosteric heats ($Q_{st}$) of $C_2H_6$ and $C_2H_4$ for **HOF-NBDA(DMA)** exhibit comparable values, 26.1 and 23.9 kJ·mol$^{-1}$ respectively, and the differential is only 2.2 kJ·mol$^{-1}$. The experimental $Q_{st}$ of $C_2H_6$ and $C_2H_4$ for **HOF-NBDA** are 23.5 and 19.9 kJ·mol$^{-1}$, and the differential grows to 3.6 kJ·mol$^{-1}$, indicating the separation performance for $C_2H_6$ and $C_2H_4$ is significantly enhanced after the structure transformation.

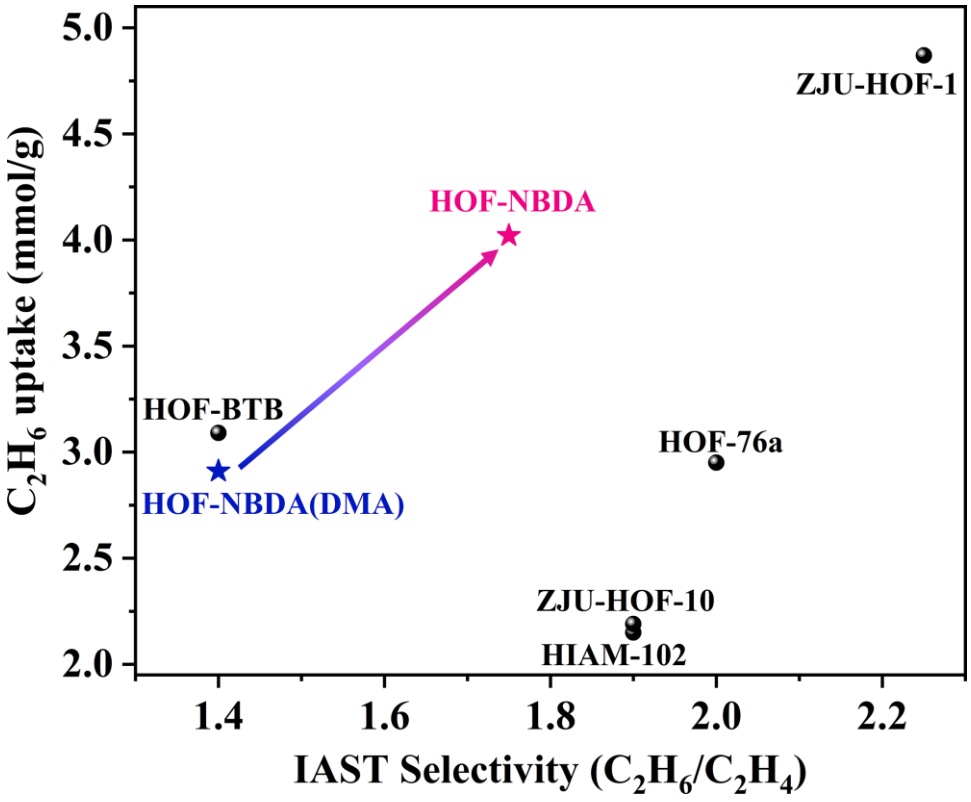


**Figure S15.** $C_2H_6$ uptake and IAST selectivity among representative reverse-order characteristic HOFs.

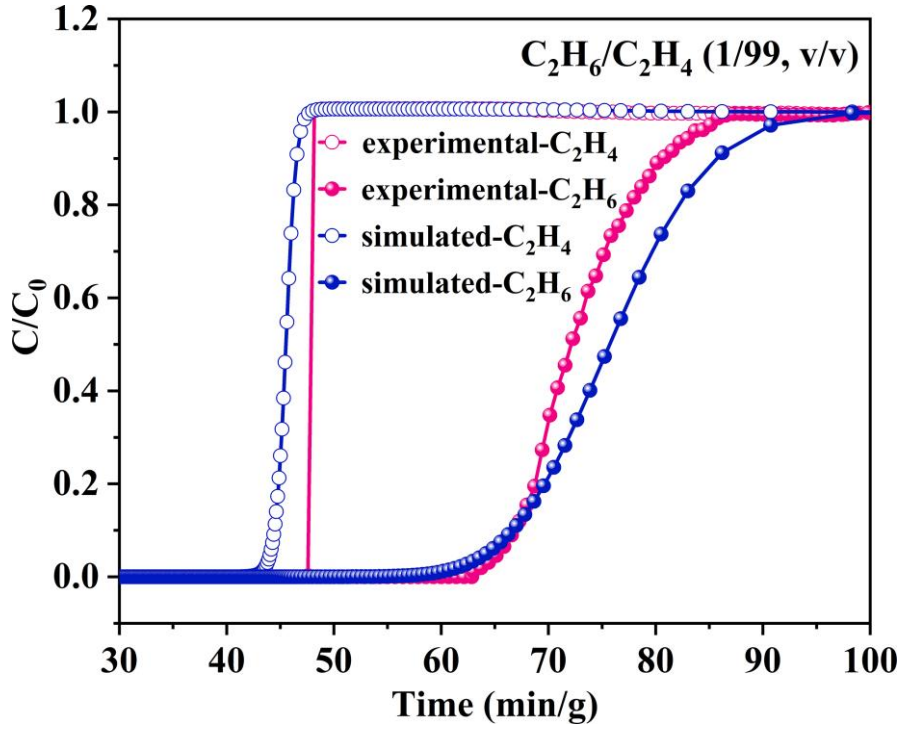


**Figure S16.** The simulated and experimental breakthrough curves with $C_2H_6/C_2H_4$ (1/99, v/v) in the **HOF-NBDA** packed column at 298 K.

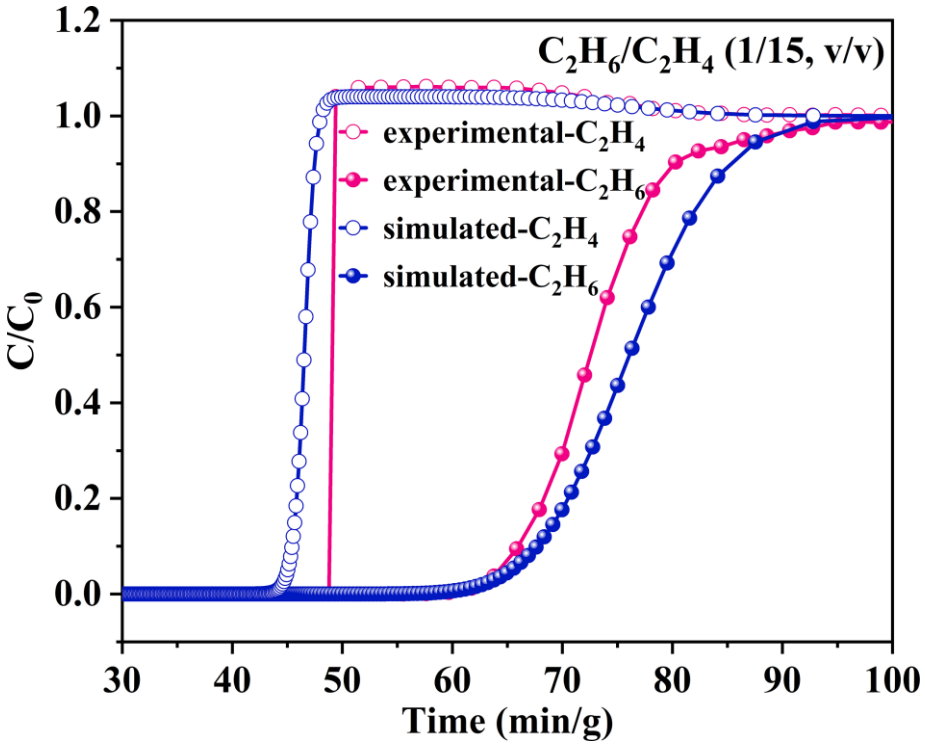


**Figure S17.** The simulated and experimental breakthrough curves with $C_2H_6/C_2H_4$ (1/15, v/v) separation in the **HOF-NBDA** packed column at 298 K.

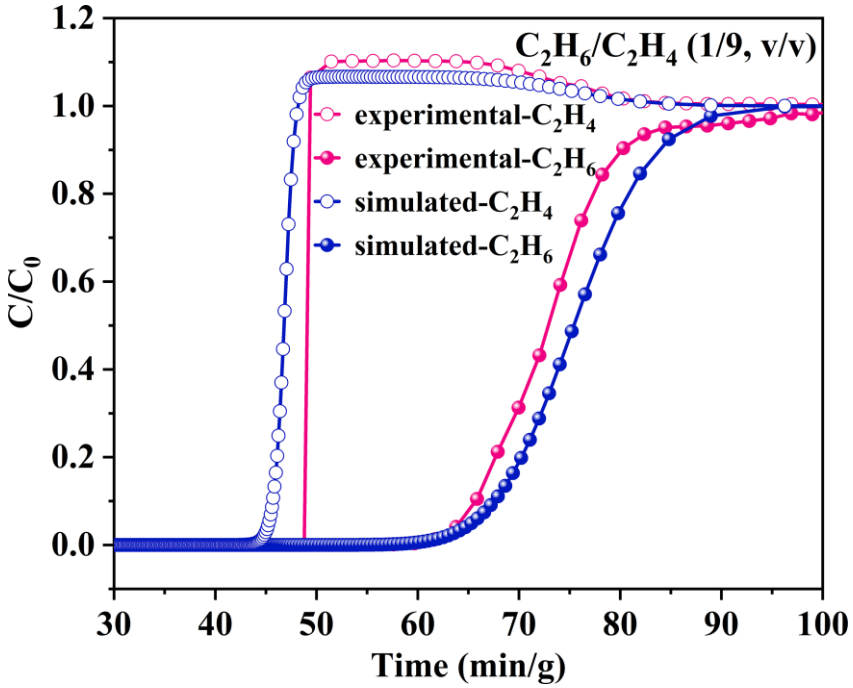


**Figure S18.** The simulated and experimental breakthrough curves for $C_2H_6/C_2H_4$ (1/9, v/v) in the **HOF-NBDA** packed column at 298 K.

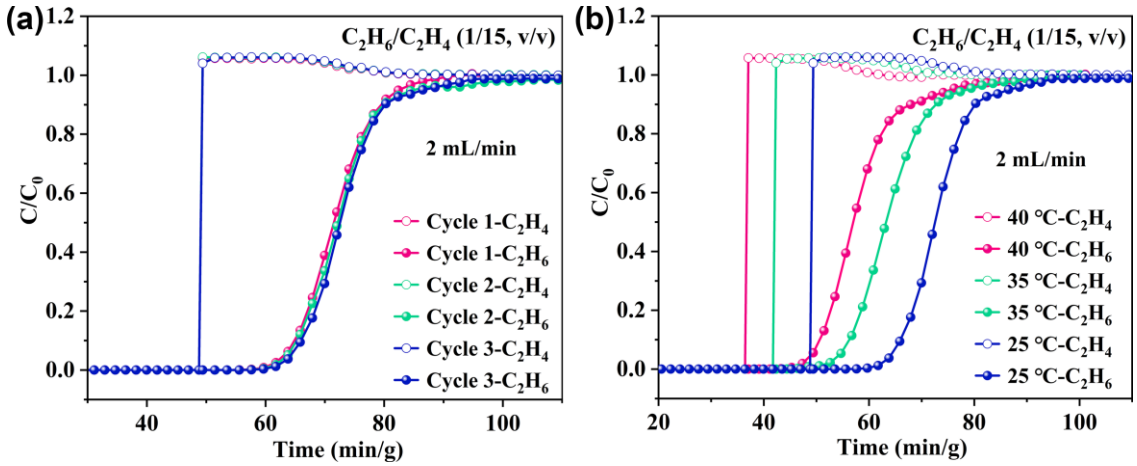


**Figure S19.** (a) The cycling breakthrough experiments for $C_2H_6/C_2H_4$ (1/15, v/v) mixture with gas flow rate of 2 mL·min$^{-1}$ at 298 K. (b) The breakthrough experiment under different temperatures with gas flow rate of 2 mL·min$^{-1}$.

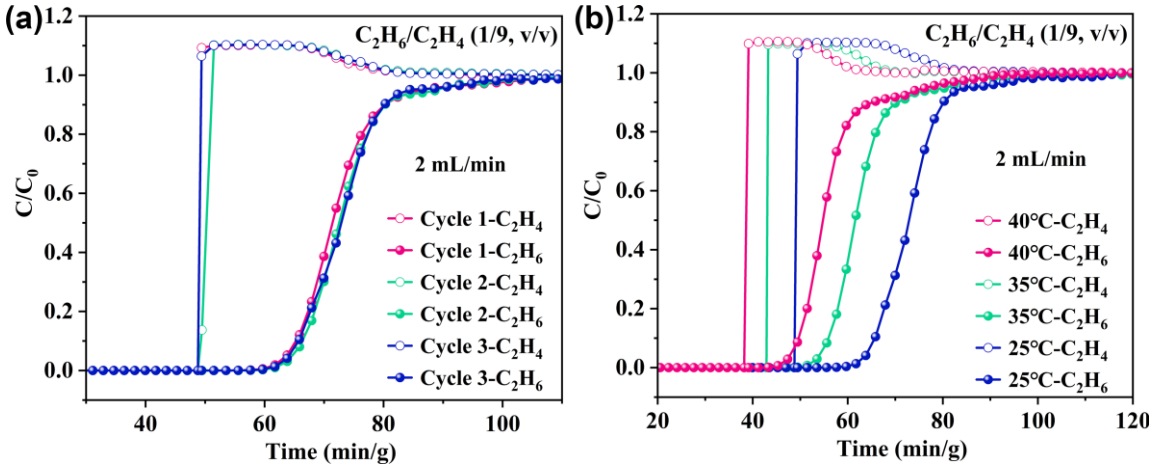


**Figure S20.** (a) The cycling breakthrough experiments for $C_2H_6/C_2H_4$ (1/9, v/v) mixture with gas flow rate of 2 mL·min$^{-1}$ at 298 K. (b) The breakthrough experiment under different temperatures with gas flow rate of 2 mL·min$^{-1}$.

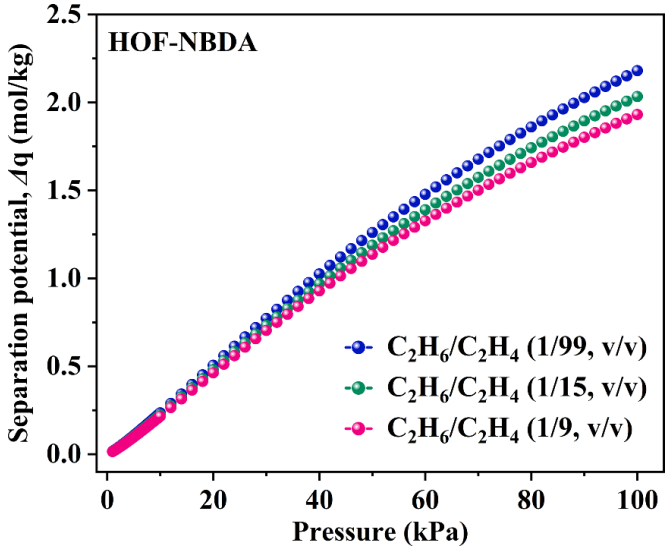


**Figure S21.** The separation potentials ($\Delta q$) of **HOF-NBDA** for different $C_2H_6/C_2H_4$ mixtures. For 1/99, 1/15 and 1/9 $C_2H_6/C_2H_4$ mixtures, the separation potentials are calculated as 2.2, 2.0 and 1.9 mol·kg$^{-1}$ respectively.

**Table S3.** Crystallographic data of **HOF-NBDA(DMA)** and **HOF-NBDA**.

| | **HOF-NBDA(DMA)** | **HOF-NBDA** |
|---|---|---|
| CCDC number | 2235806 | 2235816 |
| Empirical formula | $C_{44}H_{34}N_2O_{12}$ | $C_{42}H_{27}NO_{12}$ |
| Formula weight | 782.73 | 737.65 |
| Temperature/ K | 150 | 298 |
| Crystal system | Triclinic | Orthorhombic |
| Space group | *P*-1 | *F*ddd |
| *a*/ Å | 14.6965(3) | 14.9194(5) |
| *b*/ Å | 15.9293(3) | 28.7711(6) |
| *c*/ Å | 24.0212(3) | 49.9580(15) |
| *α*/° | 84.6990(10) | 90 |
| *β*/° | 80.9440(10) | 90 |
| *γ*/° | 68.800(2) | 90 |
| Volume/Å$^3$ | 5173.71(17) | 21444.4 (11) |
| Z | 4 | 16 |
| $\rho_{calc}$ (g/cm$^3$) | 1.005 | 0.914 |
| *F*(000) | 1632.0 | 6112.0 |
| void space /% | 31.5 | 40.5 |
| Goodness-of-fit on $F^2$ | 1.021 | 1.057 |
| $R_1$,[a] $wR_2$[b] [$I$>2sigma($I$)] | $R_1$ = 0.0781, $wR_2$ = 0.2299 | $R_1$ = 0.0470, $wR_2$ = 0.1353 |
| $R_1$,[a] $wR_2$[b] [all data] | $R_1$ = 0.0847, $wR_2$ = 0.2377 | $R_1$ = 0.0547, $wR_2$ = 0.1410 |

**Table S4.** Comparison of stabilities for some typical HOFs.

| HOF materials | Water | Acid | Thermostability | Ref. |
|---|---|---|---|---|
| **HOF-NBDA** | **√** | **√** | **~400 °C[a]** | **This Work** |
| HOF-BTB | √ | √ | ~300 °C[b] | [7] |
| HIAM-102 | √ | √ | ~250 °C[a] | [8] |
| HOF-76a | √ | √ | ~350 °C[a] | [9] |
| ZJU-HOF-1 | √ | √ | ~340 °C[a] | [10] |
| ZJU-HOF-10 | — | — | ~340 °C[a] | [11] |
| HOF-TCBP | √ | √ | ~395 °C[a] | [12] |
| HOF-4a | — | — | ~400 °C[a] | [13] |
| PFC-1 | √ | √ | ~250 °C[b] | [14] |
| Ex-1 | √ | — | ~215 °C[d] | [15] |
| 1⊂AN | √ | — | ~100 °C[a] | [16] |
| HOF-FJU-1a | √ | √ | ~250 °C[e] | [17] |
| HOF-6a | √ | — | ~350 °C[b] | [18] |
| TTBI | — | — | ~440 °C[a] | [19] |
| SOF-1a | — | — | ~420 °C | [20] |
| PFC-5 | √ | √ | ~90 °C[d] | [21] |
| HOF-GS-10 | √ | — | ~320 °C[a] | [22] |
| HOF-19a | √ | — | ~400 °C[a] | [23] |
| CPBTQ-1a | √ | × | ~360 °C[d] | [24] |
| CPHATN-1a | √ | × | ~360 °C[d] | [25] |
| PFC-25 | √ | — | ~300 °C[a] | [26] |
| CB6-H | — | √[f] | ~300 °C[d] | [27] |

[a] TGA under $N_2$ atmosphere. [b] TGA under air atmosphere. [c] TGA under Ar atmosphere. [d] VT-PXRD under air atmosphere. [e] VT-PXRD under $N_2$ atmosphere. [f] HOF material remains stable when exposed to $SO_2$.

**Table S5.** Summary and comparison of reverse-order adsorption characteristic HOFs with adsorption capacity and $C_2H_6/C_2H_4$ selectivity under ambient conditions.

| Adsorbents | IAST | $C_2H_6$ Uptake | $C_2H_4$ Uptake | $C_2H_6/C_2H_4$ uptake ratio | Ref. |
|---|---|---|---|---|---|
| HOF-BTB | 1.4 | 69.2 $cm^3 \cdot g^{-1}$ | 55.7 $cm^3 \cdot g^{-1}$ | 124% | [7] |
| (295 K) | | 3.09 $mmol \cdot g^{-1}$ | 2.48 $mmol \cdot g^{-1}$ | | |
| HIAM-102 | 1.9 | 48.25 $cm^3 \cdot g^{-1}$ | 44.39 $cm^3 \cdot g^{-1}$ | 109% | [8] |
| (298 K) | | 2.15 $mmol \cdot g^{-1}$ | 1.98 $mmol \cdot g^{-1}$ | | |
| HOF-76a | 2.0 | 66.1 $cm^3 \cdot g^{-1}$ | 37.4 $cm^3 \cdot g^{-1}$ | 177% | [9] |
| (296 K) | | 2.95 $mmol \cdot g^{-1}$ | 1.67 $mmol \cdot g^{-1}$ | | |
| ZJU-HOF-1 | 2.25 | 109 $cm^3 \cdot g^{-1}$ | ca. 89 $cm^3 \cdot g^{-1}$ | 122% | [10] |
| (298 K) | | 4.87 $mmol \cdot g^{-1}$ | 3.97 $mmol \cdot g^{-1}$ | | |
| ZJU-HOF-10 | 1.9 | 49.1 $cm^3 \cdot g^{-1}$ | 42.1 $cm^3 \cdot g^{-1}$ | 117% | [11] |
| (296 K) | | 2.19 $mmol \cdot g^{-1}$ | 1.88 $mmol \cdot g^{-1}$ | | |
| **HOF-NBDA(DMA)** | **1.40** | **65.2 $cm^3 \cdot g^{-1}$** | **60.2 $cm^3 \cdot g^{-1}$** | **108%** | **This Work** |
| **(298 K)** | | **2.91 $mmol \cdot g^{-1}$** | **2.69 $mmol \cdot g^{-1}$** | | |
| **HOF-NBDA** | **1.75** | **89.2 $cm^3 \cdot g^{-1}$** | **65.8 $cm^3 \cdot g^{-1}$** | **136%** | **This Work** |
| **(298 K)** | | **3.98 $mmol \cdot g^{-1}$** | **2.93 $mmol \cdot g^{-1}$** | | |

## Refs.


[1] R. Krishna, *RSC Adv.* **2017**, *7*, 35724-35737.

[2] R. Krishna, *Acs Omega* **2020**, *5*, 16987-17004.

[3] A. L. Myers, J. M. Prausnitz, *Aiche J.* **1965**, *11*, 121-130.

[4] R. Krishna, *Microporous Mesoporous Mater.* **2014**, *185*, 30-50.

[5] R. Krishna, *RSC Adv.* **2015**, *5*, 52269-52295.

[6] R. Krishna, *Sep. Purif. Technol.* **2018**, *194*, 281-300.

[7] T.-U. Yoon, S. B. Baek, D. Kim, E.-J. Kim, W.-G. Lee, B. K. Singh, M. S. Lah, Y.-S. Bae, K. S. Kim, *Chem. Commun.* **2018**, *54*, 9360-9363.

[8] J. Liu, J. Miao, S. Ullah, K. Zhou, L. Yu, H. Wang, Y. Wang, T. Thonhauser, J. Li, *ACS Materials Lett.* **2022**, *4*, 1227-1232.

[9] X. Zhang, L. Li, J.-X. Wang, H.-M. Wen, R. Krishna, H. Wu, W. Zhou, Z.-N. Chen, B. Li, G. Qian, B. Chen, *J. Am. Chem. Soc.* **2020**, *142*, 633-640.

[10] X. Zhang, J.-X. Wang, L. Li, J. Pei, R. Krishna, H. Wu, W. Zhou, G. Qian, B. Chen, B. Li, *Angew. Chem. Int. Ed.* **2021**, *60*, 10304-10310.

[11] J.-X. Wang, X.-W. Gu, Y.-X. Lin, B. Li, G. Qian, *ACS Materials Lett.* **2021**, *3*, 497-503.

[12] F. Hu, C. Liu, M. Wu, J. Pang, F. Jiang, D. Yuan, M. Hong, *Angew. Chem. Int. Ed.* **2017**, *56*, 2101-2104.

[13] P. Li, Y. He, H. D. Arman, R. Krishna, H. Wang, L. Weng, B. Chen, *Chem. Commun.* **2014**, *50*, 13081-13084.

[14] Q. Yin, P. Zhao, R.-J. Sa, G.-C. Chen, J. Lu, T.-F. Liu, R. Cao, *Angew.Chem. Int.Ed.* **2018**, *57*, 7691-7696.

[15] I. Hisaki, S. Nakagawa, N. Ikenaka, Y. Imamura, M. Katouda, M. Tashiro, H. Tsuchida, T. Ogoshi, H. Sato, N. Tohnai, M. Miyata, *J. Am. Chem. Soc.* **2016**, *138*, 6617-6628.

[16] D. Inokuchi, Y. Hirao, K. Takahashi, K. Matsumoto, H. Mori, T. Kubo, *J. Phys. Chem. C* **2019**, *123*, 6599-6606.

[17] Y. Yang, L. Li, R.-B. Lin, Y. Ye, Z. Yao, L. Yang, F. Xiang, S. Chen, Z. Zhang, S. Xiang, B. Chen, *Nat. Chem.* **2021**, *13*, 933-939.

[18] W. Yang, F. Yang, T.-L. Hu, S. C. King, H. Wang, H. Wu, W. Zhou, J.-R. Li, H. D. Arman, B. Chen, *Cryst. Growth Des.* **2016**, *16*, 5831-5835.

[19] M. Mastalerz, I. M. Oppel, *Angew. Chem. Int. Ed.* **2012**, *51*, 5252-5255.

[20] W. Yang, A. Greenaway, X. Lin, R. Matsuda, A. J. Blake, C. Wilson, W. Lewis, P. Hubberstey, S. Kitagawa, N. R. Champness, M. Schroeder, *J. Am. Chem. Soc.* **2010**, *132*, 14457-14469.

[21] Q. Yin, J. Lu, H.-F. Li, T.-F. Liu, R. Cao, *Cryst. Growth Des.* **2019**, *19*, 4157-4161.

[22] A. Karmakar, R. Illathvalappil, B. Anothumakkool, A. Sen, P. Samanta, A. V. Desai, S. Kurungot, S. K. Ghosh, *Angew.Chem. Int.Ed.* **2016**, *55*, 10667-10671.

[23] B. Han, H. Wang, C. Wang, H. Wu, W. Zhou, B. Chen, J. Jiang, *J. Am. Chem. Soc.* **2019**, *141*, 8737-8740.

[24] I. Hisaki, Q. Ji, K. Takahashi, N. Tohnai, T. Nakamura, *Cryst. Growth Des.* **2020**, *20*, 3190-3198.

[25] I. Hisaki, Y. Suzuki, E. Gomez, Q. Ji, N. Tohnai, T. Nakamura, A. Douhal, *J. Am. Chem. Soc.* **2019**, *141*, 2111-2121.

[26] M. Khanpour, W.-Z. Deng, Z.-B. Fang, Y.-L. Li, Q. Yin, A.-A. Zhang, F. Rouhani, A. Morsali, T.-F. Liu, *Chem. Eur. J.* **2021**, *27*, 10957-10965.

[27] J. Liang, S. Xing, P. Brandt, A. Nuhnen, C. Schluesener, Y. Sun, C. Janiak, *J. Mater. Chem. A* **2020**, *8*, 19799-19804.

## Notation

$b$ Langmuir-Freundlich constant, $Pa^{-v}$

$c_i$ molar concentration of species $i$, $mol \cdot m^{-3}$

$c_{i0}$ molar concentration of species $i$ in fluid mixture at inlet, $mol \cdot m^{-3}$

$E$ energy parameter, $J \cdot mol^{-1}$

$L$ length of packed bed adsorber, m

$m_{ads}$ mass of adsorbent packed in fixed bed, kg

$q$ component molar loading of species $i$, $mol \cdot kg^{-1}$

$q_{sat}$ saturation loading, $mol \cdot kg^{-1}$

$Q_0$ volumetric flow rate of gas mixture entering fixed bed, $m^3 \cdot s^{-1}$

$T$ absolute temperature, K